# The origin of high helium concentrations in the gas fields of southwestern Tanzania

K.M. Mtili[1] (mtili.karim@udsm.ac.tz)

D.J. Byrne[2] (david.byrne@univ-lorraine.fr)

R.L. Tyne[3] (rebecca.tyne@earth.ox.ac.uk)

E.O. Kazimoto[1] (ekazimoto@udsm.ac.tz)

C. Kimani[1] (clarahkimani@gmail.com)

C. Kasanzu[1] (kasanzu.charles@udsm.ac.tz)

D.J. Hillegonds[3] (darren.hillegonds@earth.ox.ac.uk)

C.J. Ballentine[3] (chris.ballentine@earth.ox.ac.uk)

P.H. Barry[4] (pbarry@whoi.edu)

[1]Department of Geosciences, University of Dar es Salaam, P.O. Box 35052, Dar es Salaam, Tanzania

[2]Centre de Recherches Pétrographiques et Géochimiques, UMR 7358 CNRS—Université de Lorraine, BP 20, F-54501 Vandoeuvre-lès-Nancy, France

[3]Department of Earth Sciences, University of Oxford, UK

[4]Marine Chemistry and Geochemistry Department, Woods Hole Oceanographic Institution, Woods Hole, MA, USA

# The origin of high helium concentrations in the gas fields of southwestern Tanzania

K.M. Mtili[1], D.J. Byrne[2], R.L. Tyne[3], E.O. Kazimoto[1], C. Kimani[1], C. Kasanzu[1], D.J. Hillegonds[3], C.J. Ballentine[3], P.H. Barry[4]

[1]Department of Geosciences, University of Dar es Salaam, P.O. Box 35052, Dar es Salaam, Tanzania

[2]Centre de Recherches Pétrographiques et Géochimiques, UMR 7358 CNRS—Université de Lorraine, BP 20, F-54501 Vandoeuvre-lès-Nancy, France

[3]Department of Earth Sciences, University of Oxford, UK

[4]Marine Chemistry and Geochemistry Department, Woods Hole Oceanographic Institution, Woods Hole, MA, USA

## Abstract

Volatile elements are concentrated at Earth's surface, forming a rich atmosphere and oceans which enabled the eventual emergence of life. However, volatiles are also abundant in solid Earth reservoirs, such as the crust and mantle, and these reservoirs play a key role in moderating volatile movement throughout the planet. Continental cratons represent a potentially large, yet under-constrained volatile reservoir. When cratonic regions are catastrophically disrupted by large volcanic and/or rifting events, they release massive amounts of volatiles into Earth's atmosphere on geologically-abrupt timescales (e.g., Lowenstern et al., 2014; Muirhead et al., 2020). Here, we report gas data (He-Ne-$N_2$-Ar-$CO_2$) from seeps along the flanks of the Tanzanian craton, within the western branch of the East African Rift System (EARS) - a region where the stable continental craton is actively being broken apart by rifting and simultaneously heated by plume-induced volcanism. Bulk gas and noble gas isotopic data are reported in seeps from three regions: 1) the Rukwa Rift Basin (RRB), 2) the Lupa Hydrothermal System (LHS) and 3) the Rungwe Volcanic Province (RVP). Seep gases from the RRB are dominantly comprised of $N_2$ and He, with >90% $N_2$ concentrations, high $^4$He concentrations (2.4 – 6.9%) and radiogenic He isotopes (0.16 – 0.20 $R_A$). Seeps in the LHS - located between RRB and RVP - are characterized by little-to-no $N_2$, high $CO_2$ contents (72 – 84%), relatively low He contents (0.008 – 0.15%), and higher $^3$He/$^4$He (0.95 – 0.99 $R_A$). RVP gases have high $CO_2$ (78%) and low $^4$He (0.0003%) and more mantle-like He isotopes (3.27 – 4.00 $R_A$) consistent with previous findings (Pik et al., 2006; Barry et al., 2013). All neon isotopes can be explained by mixing between air, high O/F crust and depleted Mid Oceanic Ridge Basalt (MORB) mantle-like

signatures. RVP neon isotope seep data potentially suggest a solar-like deep mantle contribution, consistent with findings in rocks from the area (Halldórsson et al., 2014), however we note that this signal is difficult to discern from mass dependent fractionation (MDF). The largest $^{40}Ar/^{36}Ar$ anomalies occur in RRB, with resolvable excess $^{40}Ar$ derived from radiogenic production in the crust. Using a noble gas solubility model, we calculate volumetric gas to water ratios ($V_g/V_w$) and show that $V_g/V_w$ values are low for RRB (0.1), consistent with longer migration distances, whereas $V_g/V_w$ are higher for LHS ($V_g/V_w$=0.1-10) and RVP ($V_g/V_w$=3-12), suggesting a more direct conduit for volatiles from source to surface. In summary, these data demonstrate interaction between two distinct helium sources, one of which is crustal in origin (most prominent in RRB) and the other being mantle-derived (enriched in RVP). The extent of mixing between the two is shown to be influenced by proximity to rift-related fault structures, groundwater interaction and magmatic heat.

**Keywords:** noble gases, helium, neon, argon, nitrogen, gas chemistry, Tanzania

## 1.Introduction

Helium is a non-renewable and naturally occurring gas that is a vital resource for several industrial and modern medical technologies. In recent years there has been a shortage in its supply, accompanied by an increase in demand (Smith et al., 2004; Grynia and Griffin, 2016; Danabalan et al., 2017). Helium and other volatile gases (e.g., $CO_2$, $N_2$) are actively released from Earth's crust and mantle in volcanically active and/or extensional rift systems (Weinlich et al., 1999; Lee et al., 2016; Brune et al., 2017; Lee et al., 2017). The East African Rift System (EARS) is an extensional intracontinental setting associated with deep volatile fluxes linked to tectonic, hydrothermal and magmatic processes (Hochstein et al., 2000; Delvaux et al., 2010; Fontijn et al., 2010). The Tanzanian section of the EARS system is characterized by substantial degassing and hydrothermal processes associated with volcanic activity and early stages of rifting in the eastern and western segments of the EARS (Lee et al., 2016; Lee et al., 2017).

Several recent studies have focused on crustal gases in Tanzania, demonstrating substantial degassing of volatiles from Earth's interior (Lee et al., 2016; Lee et al., 2017; Muirhead et al., 2020). In addition, elevated $^4He$ concentrations have previously been reported in the RRB region seeps (e.g., James, 1967; Danabalan, 2017). High $^4He$ concentration seeps have also been recently measured further north in the Manyara and Balangida regions (Danabalan, 2017;

Muirhead et al., 2020). Despite the helium potential in these basins, there have been few comprehensive studies characterizing the $^4$He distribution and accumulation mechanisms. Systematic characterization of volatiles is required to understand the overall $^4$He reservoir potential in RRB and the processes that enable formation of $^4$He rich gas seeps.

Previous studies within the western segment of the EARS, indicate contributions from both crustal and mantle volatile sources (James, 1967; Hochstein et al., 2000; Delvaux et al., 2010; Barry et al., 2013; de Moor et al., 2013; Kraml et al., 2014). Helium isotopes ($^3$He/$^4$He) are particularly useful for disentangling crustal and mantle contributions, as their endmember isotopic compositions vary by several orders of magnitude (e.g., Sano et al., 1988). Helium is inert and has two geochemically distinct stable isotopes: $^4$He, derived from radiogenic decay of U and Th, and $^3$He, a primordial nuclide trapped in the mantle during Earth's accretion (Ballentine and Lollar, 2002). Earth's crust is enriched in U and Th and thus typically exhibits a low $^3$He/$^4$He (~0.02 $R_A$; where $R_A$ is the $^3$He/$^4$He in air ($1.39 \times 10^{-6}$); Ballentine and Burnard, 2002), whereas mantle-derived gases typically range between 7-9 $R_A$ (Farley et al., 1992; Graham, 2002) with reported plume-derived $^3$He/$^4$He up to 50 $R_A$ (Ballentine and Burnard, 2002; Stuart et al., 2003; Hilton and Porcelli, 2014). Helium isotopes previously reported for the RVP, range from 0.97 to 7.2 $R_A$ (Pik et al., 2006; Barry et al., 2013). This large range is attributed to binary mixing between crustal and mantle endmembers (Barry et al., 2013; Kraml et al., 2014). In addition, these studies identified several secondary processes, such as crustal contamination, phase fractionation, thermal evolution and mineral precipitation which are responsible for the modification of the original gas seep composition in these systems (Barry et al., 2013; de Moor et al., 2013).

In this study, we use He, Ne, $N_2$, Ar, and $CO_2$ to determine the origin of volatiles in the RVP, LHS and RRB. Moreover, through geochemical modeling we explore the interaction between groundwater derived gases and crustal gases, and how this observation can explain the high flux of $^4$He across the study area, which exceeds global average steady-state production rate estimates ($3 \times 10^{10}$ atoms $^4$He $m^{-2} s^{-1}$; Tolstikhin, 1975; Mamyrin and Tolstikhin, 1984).

## 2. Geologic Setting

The RRB is located within the western branch of the EARS (Figure 1). The basin is one of a series of rift basins formed in the unique succession of half grabens, covering an area of about

3,500 km$^2$. It hosts the thickest Phanerozoic sedimentary successions in East Africa (Ebinger, 1989; Furman et al., 2004; Chorowicz, 2005; Mtelela, 2016) and is bound to the northeast by the Precambrian Tanzanian Craton (~3 Ga). It is surrounded by Proterozoic metamorphic rocks forming an area of intersection of three distinct metamorphic belts: Ubendian, Irumide and Mozambique (Harkin, 1960; De Waele et al., 2008; Kazimoto et al., 2015).

Our study area is in southwestern Tanzania, located within the NW-SE trending segment of the Paleoproterozoic Ubendian belt (Figure 1). The belt can be subdivided into lithological distinct crustal blocks, bounded by steeply dipping shear zones (Daly, 1988; Delvaux et al., 2013). Samples were collected within the Mbozi Block, which is composed of metabasite, granulites and quartzite (Daly, 1988). These rocks are overlain by the Late Carboniferous-Permian Karoo Red Sandstone Group. The latter are overlain by an unconformity and the Cretaceous Galula Formation and the Oligocene Nsungwe Formation, which are composed of sandstones, conglomerates and mudstones (Roberts et al., 2010). Neogene lake beds composed of conglomerates, siltstones, mudstones, volcaniclastic rocks and organic-rich sediments overlay the Galula Formation (Delvaux et al., 2010; Mtelela, 2016).

Geologic structures in the RRB developed mainly through reactivation of older Neoproterozoic sinistral shear zones within the Ubendian Belt during the Phanerozoic era (Delvaux, 2001). To the southwest, the RRB is bounded by the Ufipa fault, and to the northeast by the Lupa Border fault, which is associated with the distribution of LHS seeps. To the south, the basin bifurcates into the Songwe half-graben and Msangano trough, which is separated from Songwe trough by the Mbozi plateau (Heilman et al., 2018). The volcanic deposits of RVP bind the RRB in the southeast end of the basin. Furthermore, the RVP is bounded to the northeast by the poorly developed NE-trending Usangu rift basin, where Permo-Triassic to Neogene sediments overlie the Precambrian basement.

Rifting and magmatism are coeval in the RVP, dating back to ~8.6 Ma (Harkin, 1960; Ebinger et al. 1989). Volcanism and related hydrothermal activity is distributed into three major volcanic centers: Rungwe, Ngozi and Kiejo (Kyejo) as well as smaller, possibly monogenetic, eruptive centers (Chorowicz, 2005; Fontijn et al., 2010, 2012). These eruptive centers are characterised by older phonolitic basalts (~7.2 Ma), trachyte lava/tuff and Late Pliocene to Pleistocene

volcanoclastic deposits (Harkin, 1960; Ebinger 1989; Crabtree and Chesworth, 1992; Hochstein et al., 2000; Fontijn et al., 2010).

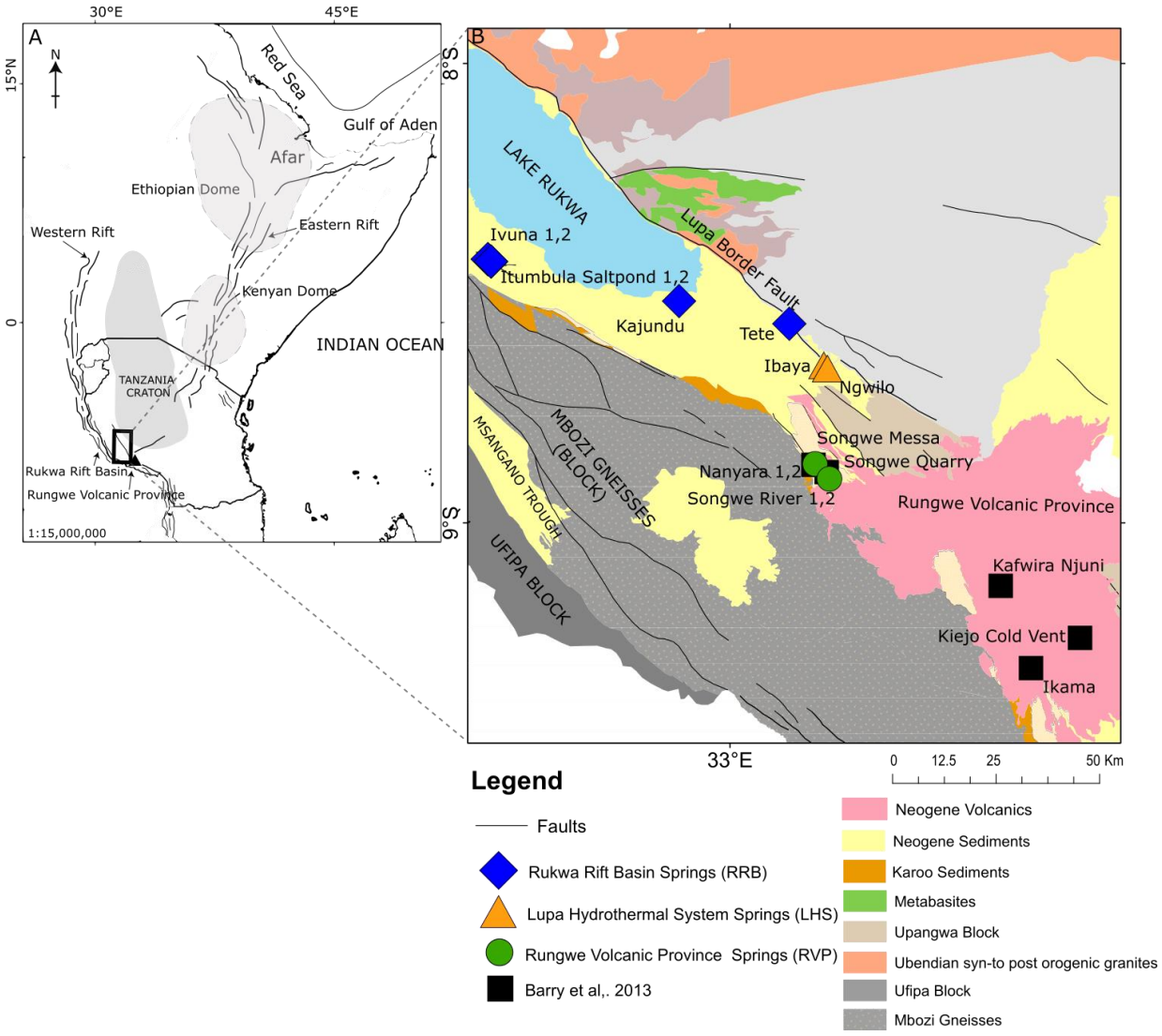


**Figure 1. 1**A-Location of the EARS, RRB, LHS and RVP (after Chorowicz, 2015). 1B-Zoomed in map of study area from insert map in Figure 1a with sample locations, fault system and geology of the area. Sample locations from Barry et al., (2013) have been added for reference.

## 2.1. The Hydrothermal Systems and Volatiles in the RRB, LHS and RVP

Gas seeps occur throughout the RRB, LHS and RVP regions. Seeps are most prevalent along streambeds, riverbanks, faults, joints and their intersections, which allows for gas migration from subsurface volatile reservoirs, associated with both high and low temperature hydrothermal activity (James, 1967; Hochstein et al., 2000; Kervyn et al., 2006; Delalande et al., 2008, 2011;

Barry et al., 2013; de Moor et al., 2013). This study aims to geochemically categorize these degassing seeps (i.e., springs) from three areas. The RRB seeps (n= 10) are found near the middle of the Rukwa basin, southeast of Lake Rukwa. They are characterized by temperatures ranging from 29.5 to 50.1 °C and relatively low salinity water (electrical conductivity = 1477 – 6247 $\mu S^{-1}$) (Table 1b; Hochstein et al., 2000). The LHS seeps (n=4) occur along the Lupa Border fault on the eastern side of the rift basin and are bounded by the Tanzanian craton (Figure 1). These seeps are characterized by higher gas fluxes, high temperature (54.6-81.7 °C) and relatively stable salinities (3138-3204 $\mu S^{-1}$). The RVP seeps (n=4) are located in the Ngozi-Songwe hydrothermal system, a subgroup of the RVP hydrothermal system, approximately 145 km SW of Lake Rukwa (Delalande et al., 2011). These seeps are also located along streambeds and riverbanks, characterized by intermediate gas fluxes, saline waters (3805-4045 $\mu S^{-1}$) and temperatures between 38.6 and 56.0 °C (Table 1). RVP seeps have previously been shown to have discharge rates of ~5-70 l/s (Hochstein et al., 2000), however little is known about discharge rates in LHS and RRB. The Ngozi volcano (the closest volcanic centre) allows for groundwater recharge, forming the hydrothermal system in the Songwe valley, an interpretation consistent with the geothermal model presented by Delvaux et al., (2010). All seeps are associated with fault systems, linked to the deep basement aquifer system, and accompanied by variable gas flux rates. James (1967) suggested, from variable enrichments of Na/K and chlorides in the water, that these seeps may originate from heating of deep circulating groundwater. However, we note that salinities are not correlated with He isotopes, so cannot be considered a diagnostic feature of volatile source depth.

## 3.Sampling and Analytical Techniques

### 3.1.Bulk Gas Measurements

Bulk gas measurements (n=9) were conducted on gases collected across the study area. Samples were collected by submerging and inverting water-filled 500 ml glass beakers over seeps, allowing sample gases to displace the water and thus avoiding atmospheric contamination. A 20 $cm^3$ syringe was then inserted into the still-submerged gas-filled beaker to withdraw the sample gas. The extracted gas was then transferred to a 0.25 L foil sample bag (Cali-5-Bond™), whilst the sample bag was submerged, to ensure no atmospheric contamination.

A field-based portable quadrupole mass spectrometer (MiniRuedi) was used to analyse the bulk gas composition (He, Ar, $N_2$ and $CO_2$) of the samples within a few hours of collection

(Brennwald et al., 2016; Sundal et al., 2020). Each sample bag was attached to one of six inlet ports, each fitted with a needle connection and leading to a multiport valve; this valve was connected via a 10 m long 0.1 mm inside diameter capillary to the MiniRuedi ion source volume. When each sample port was opened, gases were dynamically drawn through the system and signals were measured on a quadrupole mass spectrometer by peak jumping. $N_2$, $O_2$, $CO_2$ and Ar were measured over five cycles on the Faraday cup, and $^4He$ was then measured over 10 cycles on the multiplier (Brennwald et al., 2016). Samples were calibrated against air standards, either collected in a gas bag away from possible contamination or as ambient air in a well-ventilated room, and measured with protocols identical to samples. Samples and standards were measured sequentially to minimise variations due to atmospheric pressure. Line blanks were analysed after every 5 samples, to ensure there was no memory effect within the extraction system or mass spectrometer.

### 3.2. Noble Gases Sampling and Analysis

Noble gas samples (n=21) were collected in copper tubes using standard techniques (e.g., Weiss 1968; Kennedy et al. 1985). In brief, the copper tube was connected to a funnel with Tygon® tubing. The funnel was then inverted and placed on top of the seep to collect the bubbles as they emanated from the seep. The other end of the copper tube was fitted with a second piece of Tygon® tubing, connected to a second copper tube and a third piece of Tygon® tubing, which was submerged in a water container to ensure no backflow of air. The duration of sampling ranged from 1 to 8 hours depending on the flux (bubbling rate) of the seep. More time was required for air to be sufficiently flushed out of the system when seeps had low flow rates. Copper tubes were crimped using specially designed stainless steel clamps and sealed at both ends, effectively trapping seep gases between the clamps within the copper tube.

Copper tubes were then transferred back to the Noble Laboratory at the Department of Earth Sciences, University of Oxford. The laboratory is equipped with a dual mass spectrometer and purification system (Barry et al., 2016, Tyne et al., 2019). Samples were interfaced with a purification system and expanded into a known volume where the pressure was recorded on a Baratron® capacitance manometer. By determining the pressure within a known volume, the total number of moles of a given gas was calculated by comparing sample signals on the mass spectrometer with air standard signals using an identical purification procedure. In this way, noble gas concentrations were calculated for all unknown samples. Noble gases were isolated by

initially transferring the gas onto an activated titanium sponge held at 950 $^{o}$C, this was subsequently cooled to room temperature in order to remove reactive gases. The gases were then expanded into dual hot/cold getter volume (SAES GP-50 at 250 $^{o}$C, SAES NP-10 at room temperature) for 10 minutes, for further removal of reactive gases. A sub-aliquot of gas was isolated and inlet into a Hiden Analytical Hal-201 quadrupole mass spectrometer for preliminary quantitation of noble gases. The noble gases were then cryogenically trapped onto a stainless steel trap at 15K (Ar-Kr-Xe) and charcoal trap at 10-15K (He and Ne). By successively raising the temperature in the traps, He was first released and measured on ThermoScientific Helix SFT and the remaining noble gases were measured sequentially on a ThermoScientific Argus VI following the methods of Barry et al., (2016) and Tyne et al., (2019).

Air standards and blanks were run regularly using a similar procedure, to monitor changes in machine sensitivity. Blank contributions were less than 2% of the typical sample signal. During Ne measurements, the $^{40}$Ar peak was also measured in order to correct for interference of $^{40}Ar^{++}$ on the $^{20}$Ne peak, following Niedermann et al. (1993).

## 4.Results

Bulk gas composition and the noble isotope data of RRB, LHS and RVP can be found in Table 1a. Springs north of S 08°35' are classed as RRB, springs located between S 08°35' and S 08°45' are grouped as LHS and those located south of 08°45' are classed as RVP (Figure 1). RVP data are reported in detail in Kimani et al. (2021). Geochemical trends are distinct between these geographical groupings, however we note that samples Kajundu and Tete fall towards the southern edge of the RRB sample group, and show some signatures closer to the LHS sample group than to the rest of the RRB samples, further to the north.

### 4.1.Bulk gas composition

The three sampling regions each have distinct $N_2$-He-Ar-$CO_2$ seep compositions (Figure 2; Supplementary Figure 2 and 3; Table 2), as measured in the field using the MiniRuedi portable mass spectrometer. Seeps in the RRB, have $N_2$ contents ranging between 93% and 95% and low $CO_2$ contents (0.80 and 2.1%). The Ibaya and Ngwilo seeps within the LHS, have lower $N_2$ concentrations (14 to 24%) and high $CO_2$ concentrations (72.4% −to 83.7%). The RVP hydrothermal system also has low $N_2$ concentrations (18-19%) and high $CO_2$ concentrations (77.6%).

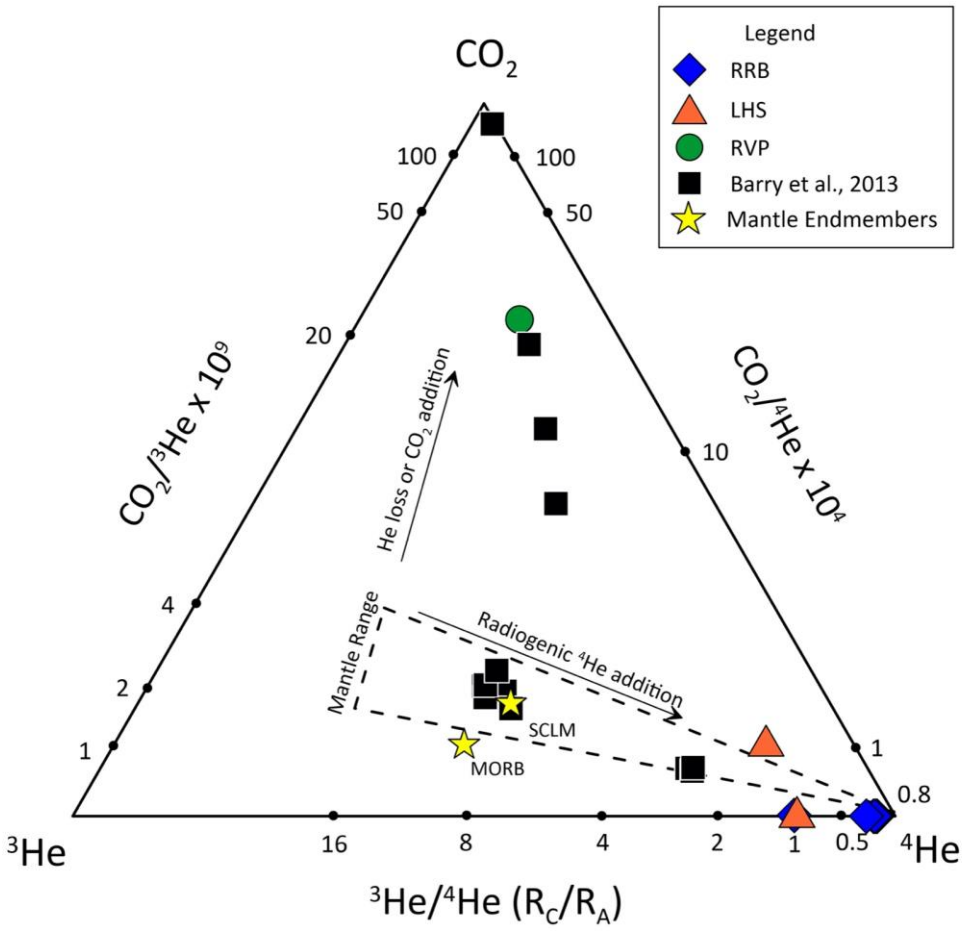


**Figure 2.** $CO_2$-$^4$He-$^3$He Ternary plot for the RRB, RVP and LHS seeps. Endmember mantle compositions (yellow stars) and expected trends (dashed lines/arrows) are shown. 1 sigma errors are within the symbol size. Samples from the RRB hydrothermal system plot close to the $^4$He apex due to the fact that these samples are extremely He-rich, whereas RVP data plot nearer to the $CO_2$ apex reflecting the increased mantle volatile contribution. Previously published compositional data from the RVP (Barry et al., 2013) are plotted for reference and are in agreement with the new RVP data (Kimani et al., 2021). Helium data in this figure were analyzed from samples collected in copper tubes for noble gas isotopes (Section 3.2) while $CO_2$ data were analysed for bulk gas geochemistry using a field-portable mass spectrometry system (Section 3.1).

## 4.2.Noble gas isotope composition of seeps

### *4.2.1.Helium*

Seep samples from the RRB hydrothermal system have high $^4$He concentrations ($2.2 \times 10^{-3}$ to $6.9 \times 10^{-2}$ cm$^3$ STP/cm$^3$). The Itumbula and Ivuna seeps, within RBB, have the highest $^4$He concentrations ($2.4 \times 10^{-2}$ and $6.9 \times 10^{-2}$ cm$^3$ STP/cm$^3$ (2.4-6.9%) and have radiogenic helium isotope values (0.16−-0.19 $R_A$; Table 1a). The Kajundu and Tete (southern RRB) have lower $^4$He concentrations ($2.2 \times 10^{-4}$ cm$^3$ STP/cm$^3$ (0.02%) and $7.6 \times 10^{-3}$ cm$^3$ STP/cm$^3$ (0.76%), respectively) and higher helium isotope ratios of 0.99 $R_A$ and 0.26 $R_A$, respectively.

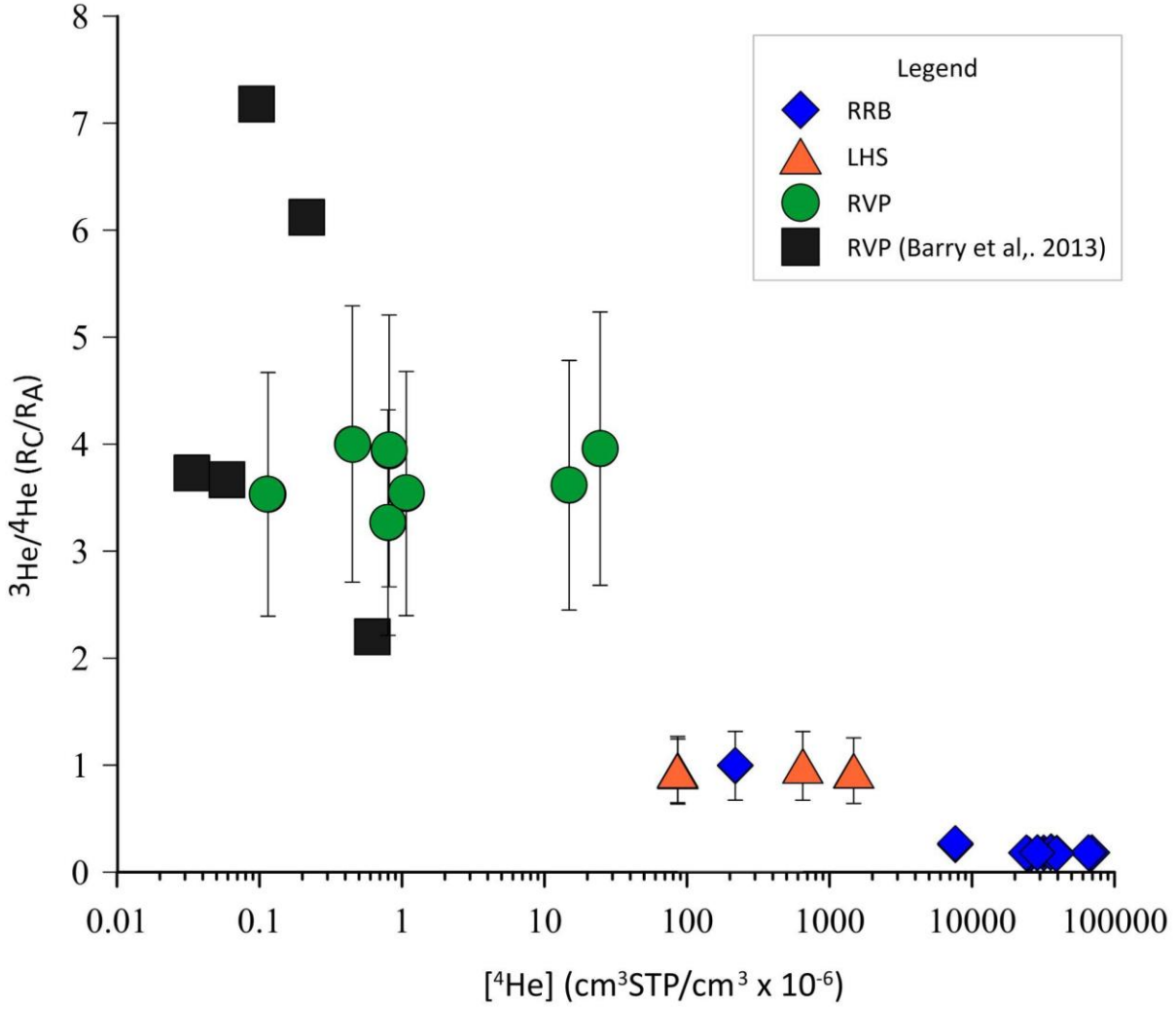


**Figure 3.** Air corrected helium isotope ratios as a function of helium concentration. A clear negative correlation is evident, showing that the highest $^4$He content samples are associated with the lowest He isotope ratios. 1 sigma error bars in the data are shown, where absent errors are within symbol size. RVP data (green symbols) are from Kimani et al., (2021). Black squares

represent data from Barry et al., (2013). All data in this figure were analyzed from samples collected in copper-tubes for noble gas isotopic measurements.

Seeps from the LHS (i.e., Ibaya and Ngwilo) have lower $^{4}He$ concentrations ($8.6 \times 10^{-5}$ to $1.5 \times 10^{-3}$ $cm^3STP/cm^3$ (0.0086-0.15%) respectively) and air corrected $^{3}He/^{4}He$ values between 0.94-0.99 $R_A$. The $^{4}He$ content in RVP ranges from $1.2 \times 10^{-7}$ to $2.5 \times 10^{-5}$ $cm^3STP/cm^3$ (Kimani et al., 2021). Air corrected $^{3}He/^{4}He$ values in the same RVP seeps range between 3.27 and 4.00 $R_A$ (Kimani et al., 2021). Notably, $^{3}He/^{4}He$ values increase systematically from the RRB towards the RVP in the south (Table 1a). The $^{4}He/^{20}Ne$ values for the samples range between ~1 and 15,000, suggesting limited atmospheric contributions to most samples (Table 1a).

### *4.2.2. Neon*

RRB samples have high $^{20}Ne$ concentrations ranging between 3,090 and 12,100 $\times 10^{-9}$ $cm^3$ $STP/cm^3$ (Table 1a), whereas $^{20}Ne/^{22}Ne$ values vary from 9.64 to 9.77 and $^{21}Ne/^{22}Ne$ ranges between 0.028 and 0.033 for RBB samples (Figure 4). The majority of gas seeps are consistent with air mixing with radiogenic neon derived from high O/F crust (Figure 4). Samples from the RVP have $^{20}Ne$ concentrations between 8.52 and 82.3 $\times 10^{-9}$ $cm^3$ $STP/cm^3$, with $^{20}Ne/^{22}Ne$ ranging from 9.83 to 9.99 (Kimani et al., 2021) and $^{21}Ne/^{22}Ne$ has a tight range of 0.02835 to 0.02938. These RVP signatures plot close to the solar-air mixing line, suggestive of a primordial neon component that is observed in deep plume-source mantle (Broadley et al., 2020). Such a component would be consistent with the higher $^{3}He/^{4}He$ ratios observed in this area, however we note that this trend is difficult to discern from mass dependent fractionation (MDF). In contrast, gas seeps from the LHS do not indicate any clear trend in Ne isotope space, with $^{20}Ne/^{22}Ne$ ranging from 9.78 to 10.01 and $^{21}Ne/^{22}Ne$ from 0.0276 to 0.0296 (Figure 4; Table 1b). $^{20}Ne$ concentrations range from 41.8 to 1,090 $\times 10^{-9}$ $cm^3$ $STP/cm^3$.

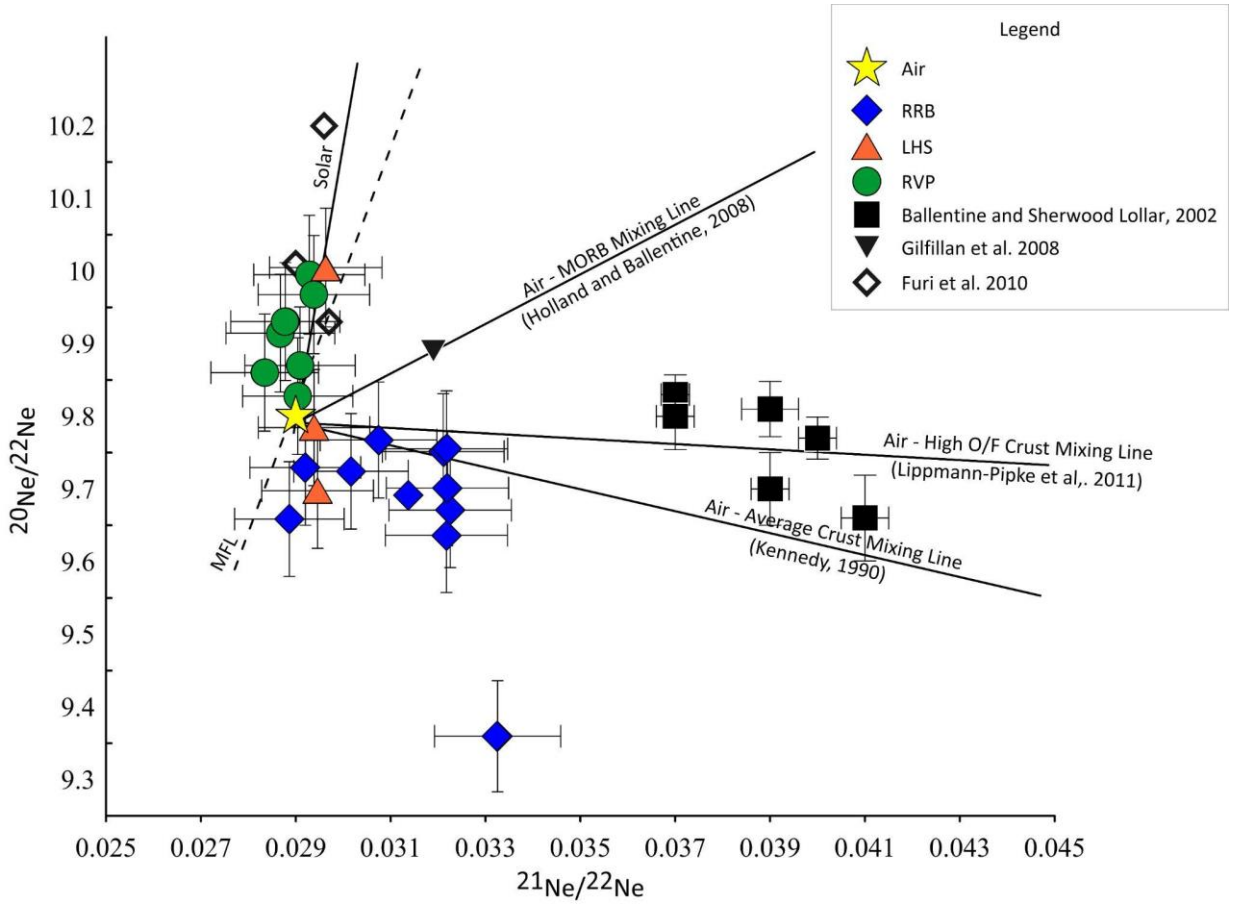


**Figure 4.** Neon three isotope ($^{20}$Ne, $^{21}$Ne and $^{22}$Ne) plot illustrating mixing between air and solar (Sarda et al., 1988), air and MORB (Ballentine and Holland, 2008), air and high O/F crust (Archean) (Lippmann- Pipke et al., 2011) and air and average crust (Kennedy et al., 1990). Also shown is a broken line denoting the line along which mass dependent fractionation would occur (MFL). Errors are calculated at the 1 sigma level. All data in this figure were analyzed from samples collected in copper-tubes for noble gas isotopic measurements at Oxford University.

### *4.2.3. Argon*

Argon concentrations are highest in the RRB (3,100 to 15,400 × $10^{-6}$ $cm^3$ STP/$cm^3$) compared to between 74.9 and 1,770 × $10^{-6}$ $cm^3$ STP/$cm^3$ in LHS and 11.7 and 89.4 × $10^{-6}$ $cm^3$ STP/$cm^3$ in the RVP (Kimani et al., 2021; Table 1a). $^{40}$Ar/$^{36}$Ar values in the RRB are between 298 and 847 and indicate a resolvable excess radiogenic $^{40}$Ar ($^{40}$Ar*) relative to air ($^{40}$Ar/$^{36}$Ar$_A$ = 298.56; Lee et al., 2006). The LHS seeps have $^{40}$Ar/$^{36}$Ar values slightly higher than air (306 to 369; Table 1a) whilst $^{40}$Ar/$^{36}$Ar values in the RVP are between 301 and 369 (Kimani et al., 2021; Table 1a).

#### *4.2.4.Krypton and xenon*

Measured $^{84}Kr$ concentrations range from 1.49 to 474 × $10^{-9}$ $cm^3STP/cm^3$ and measured $^{132}Xe$ concentrations are between 124 and 34,400 × $10^{-12}$ $cm^3STP/cm^3$. $^{84}Kr$ and $^{132}Xe$ isotope ratios are air-like and are not further considered in this study.

## 5. Discussion

In the following discussion, we investigate the sources and processes controlling noble gas isotopes and gas chemistry in southwestern Tanzania. We explore mixing scenarios between crustal and mantle sources and the underlying tectonic and thermal controls on volatile release and transport. We present a quantitative solubility exchange model predicting volumetric gas to water ratios ($V_g/V_w$), which can be used to explain high $^4He$ concentrations in seeps. Finally, we calculate crustal $^4He$ fluxes for each region and demonstrate that they are significantly higher than regional steady-state crustal production estimates.

### 5.1. Relative abundances of gases in southwestern Tanzania

#### *5.1.1 $^4He/^{40}Ar$*

Mantle gases typically have $^4He/^{40}Ar$ production ratios between 1.4 and 4.8 (Matsuda and Marty, 1995), whereas crustal gases have $^4He/^{40}Ar$ production ratios between 4.1 and 8.9 (Warr et al., 2019), which are both significantly higher than air (~5.6 × $10^{-4}$) and ASW (~1.2 × $10^{-4}$) (Burnard et al., 1997; Zimmer et al., 2004: Kipfer et al., 2002).

The measured $^4He/^{40}Ar$ value decreases from north to south, from RRB (~2.8) to LHS (~0.7) to RVP (0.04). All samples have $^4He/^{40}Ar$ values significantly higher than air (~5.6 × $10^{-4}$). With the exception of Kajundu, where the bulk gas measurements appear to be air contaminated, the RRB samples have $^4He/^{40}Ar$ values in the mantle production range and very close to the crustal production range. The LHS and RVP seeps have values $^4He/^{40}Ar$ values below the mantle and crustal production ranges, consistent with degassing of a mantle-like endmember (Kimani et al., 2021). Alternatively, samples could be pervasively diluted by small air contributions, with the RBB samples mixing with a radiologically-enriched end-member, thus retaining higher observed $^4He/^{40}Ar$ values. Migration (from source to seep) can also potentially fractionate noble gases, either during dissolution and exsolution in groundwater, or by mass-dependent fractionation during diffusion through porous media.

### *5.1.2. $N_2/^{40}Ar$*

$N_2/^{40}Ar$ is known to vary between subsurface-derived gases of different sources, with a compilation by Marty & Dauphas (2003) showing different values for MORB-like (124±40), plume-like (74±34) and continental crust-like signatures (300±100). Notably, the $N_2/^{40}Ar$ of air (83) and ASW (40) overlap with that of plumes (Giggenbach 1996; Marty and Zimmermann, 1996; Fischer et al., 1998; Marty and Dauphas, 2003; Figure 2). Fischer et al. (2005) reported relatively high $N_2$/Ar from the subcontinental lithospheric mantle (SCLM; 234±144), suggesting that crustal sources are consistently rich in $N_2$. In this study, we observe differences between samples from RRB, LHS and RVP (Figure 2) which suggest variable mantle and crustal volatile contributions.

With the exception of Ivuna, the $N_2/^{40}Ar$ in the seeps are greater than air (83) (Figure 2) and appear to decrease away from the volcanic center, with approximate values of ~2,000 in RVP, ~1000 in LHS and ~100 in RRB. The decrease of $N_2/^{40}Ar$ across the rift basin away from the volcanic center indicates either lower $N_2$ contents or higher excess $^{40}Ar$ ($^{40}Ar^*$; Eq. 2) in samples further from the RVP. Notably, both $N_2$ and $^{40}Ar$ concentrations decrease from north to south, which suggests a greater radiogenic input in RRB than in LHS and RVP (Table 1a and 2).

### *5.1.3. $N_2/^4He$*

The $N_2/^4He$ value of the mantle (~150; Labidi et al., 2020) is significantly higher than crustal values (1.9 to 5.1; Labidi et al., 2020) and significantly lower than the atmospheric value of ~1.5 × $10^5$.

The $N_2/^4He$ value increases from north (RRB ~45) to south (LHS ~896 and RVP ~7,460). This is the result of a decrease in $N_2$ concentrations as the system moves from predominantly crustal to mantle. The seeps from RRB have $N_2/^4He$ signatures consistent with a significant input of a crustal endmember, although the Tete seep within RRB is an exception, with a $N_2/^4He$ value of 118. This may be due to the nearby border fault, which could act as a conduit providing greater mantle contributions (Figure 1). We note that seeps from LHS and RVP have $N_2/^4He$ values (~896 and ~7,460 respectively) significantly greater than the mantle value. Such high $N_2/^4He$ values have previously been reported in volcanic arc settings (1,870±15; Giggenbach, 1996; Fischer et al., 1998; Sano et al., 2001) and are attributed to the preferential recycling of $N_2$ relative to He, however it can explain the values in the EARS as it is far from any modern subduction zone. Nevertheless, if ancient subduction has metasomatized the mantle, such high

$N_2/^4He$ signatures could be retained in the mantle source, as $N_2$ is preferentially recycled relative to He, resulting in a metasomatically $N_2$ enriched mantle source (Barry and Hilton, 2016; Fischer and Foley, 2017; Aiuppa et al., 2021; Barry and Broadley, 2021; Bekaert et al., 2021). Alternatively, samples could be $N_2$ rich due to incorporation of $N_2$ during gas emplacement - there are abundant nitrogen-rich sediments in the subsurface beneath the EARS and $N_2$ rich cratonic material has formed in the region from the amalgamation of multiple paleo-arc environments (Smirnov et al., 1973, Sklyarov et al., 1998, Boniface and Schenk, 2012, Boniface et al., 2012, Boniface and Tsujimori, 2019).

### *5.1.4. Relation between $N_2$-$^{40}Ar$-$^4He$-$CO_2$ and lithotectonics of southwestern Tanzania*

High $CO_2$ concentrations are associated with LHS and RVP samples, likely due to their proximity to the volcanic provinces. The contribution of mantle volatiles (e.g., $CO_2$) to a hydrothermal system has been shown to increase with proximity to the volcanic center (Barry et al., 2013; de Moor et al., 2013; Kraml et al., 2014). Within the RVP, volatiles are thought to be sourced from the flanks of the Ngozi Volcano (i.e., the closest volcanic source, located ~40 km to the southeast of the study area) through fault controlled migration (Delvaux et al., 2010; Kraml et al., 2014).

In the RRB, $^4He$ concentrations are much higher than in the RVP, and $N_2$ appears to be the dominant carrier gas (Table 1). Radiogenic $^4He$ is likely sourced from the Mbozi basement rock (i.e., metamorphosed granitic rock, rich in radioelements U and Th) and high $^4He$ concentrations in RRB gases are likely facilitated by thick rock seals (i.e., lake beds) which allow crustal gases to accumulate (analogous to the way hydrocarbons accumulate in sedimentary basins). Seismic data shows a decrease in lake bed (effective seal) thickness from RRB (>4 km) towards RVP (~2 km), which may result in variable $^4He$ contributions to the system and low accumulation of $^4He$ in regions without effective seals (Wescott et al., 1991; Kilembe and Rosendahl 1992; Morley et al., 2000). The observed high $N_2$ in RRB (compared to LHS and RVP) is thought to be influenced by low grade metamorphism of basement rocks, $N_2$-rich cratonic material and/or thick meta-sediments within RRB. While the source of $N_2$ remains somewhat enigmatic, these findings are consistent with the reported association of $N_2$ and crustal-sourced $^4He$ in gas fields (Zartman et al., 1961; Weinlich et al., 1999; Ballentine and Sherwood-Lollar, 2002; Gilfillan and Ballentine, 2018). Future studies should characterize the nitrogen isotopes in these seep gases in order to better constrain the source(s) of nitrogen.

## 5.2 Helium, neon and argon isotope systematics

### *5.2.1 Helium sources and binary mixing models*

Noble gases in natural systems are in most cases sourced from a mixture of crustal and mantle components, which are ultimately controlled by the regional geology and tectonic regime of the gas system. Crustal and mantle helium isotope endmembers have different helium isotope ratios (0.02 $R_A$ and 8±1 $R_A$ respectively (Ballentine and Burnard, 2002; Graham, 2002)), which permit calculation of the fraction of each endmember:

$$R_{sample} = f_{mantle}R_{mantle} + f_{radiogenic}R_{radiogenic} \quad (1)$$

where R denotes the air-normalized He isotope ratio ($^3He/^4He$) and $f$ is the fraction in a given sample. A systematic increase in mantle contribution ($f_{mantle}$) towards the volcanic center is observed.

The mantle helium contribution in the RRB seeps is ~ 2% consistent with a dominantly radiogenic origin (Table 1), its position above older basement rocks of the Ubendian Belt (Lenoir et al., 1994; Danabalan, 2017) and the high $^4He$ concentrations in the region (up to 6.9%; Table 1). Moreover it is in agreement with findings from Ebinger (2005), who suggested the RBB is undergoing early stages of rifting and lithosphere thinning, but not experiencing significant mantle inputs. The proximity to the Cenozoic volcanism in the RVP likely provided the necessary heating for the release of accumulated radiogenic He (King and Metcalfe, 2013). Several deep faults are present in the basin and we suggest that Ivuna and Itumbula (RRB), which have the highest $^4He$ and $^{40}Ar^*$, may be connected to axial Itumbula rift faults, which focus radiogenic volatiles ($^4He$ and $^{40}Ar$) in the respective hydrothermal systems (Heilman et al., 2018; Figure 1; Supplementary Figure 1a).

The LHS gas seeps have higher mantle He contributions ($f_{mantle}$) of ~12% versus those from the RRB consistent with the lower $^4He$ concentrations and higher $CO_2$ concentrations. The proximity of the LHS seeps to the Lupa Border Fault, which permeates to the basement, provides a mechanism for enhanced release of deep crustal $^4He$ and subsequent mixing with shallow (crust) and deep (mantle) components (Supplementary Figure 1b). The RVP seeps have an increased mantle contribution ($f_{mantle}$) between 49-90%, consistent with their location closest to the Ngozi volcanic center and furthest from the radiogenic sources in the RRB.

### *5.2.2 Coupled He and Ne isotopes*

RVP samples show elevated $^{20}Ne/^{22}Ne$ values relative to the atmospheric value (Figure 4). This may be indicative of neon contributions from a deep mantle (i.e., solar) source (Williams and Mukhopadhyay, 2019), consistent with findings in rocks from the area (Halldórsson et al., 2014), however we note that we cannot discern this signal from mass dependent fractionation (MDF). Samples displaying high $^{21}Ne/^{22}Ne$ (i.e., in the RRB) are correlated with the most crustal-like samples in the study (Figure 5;Figure 6). RBB samples clearly have lower $^{20}Ne/^{22}Ne$ and higher $^{21}Ne/^{22}Ne$, consistent with a larger contribution of crustal radiogenic Ne (Lippmann-Pipke et al., 2011) and higher radiogenic $^{4}He$ contributions. Whereas the lowest $^{21}Ne/^{22}Ne$ values and $^{4}He$ concentrations are in the RVP, with the LHS having intermediate values (Figure 5; Figure 6, Table 1).

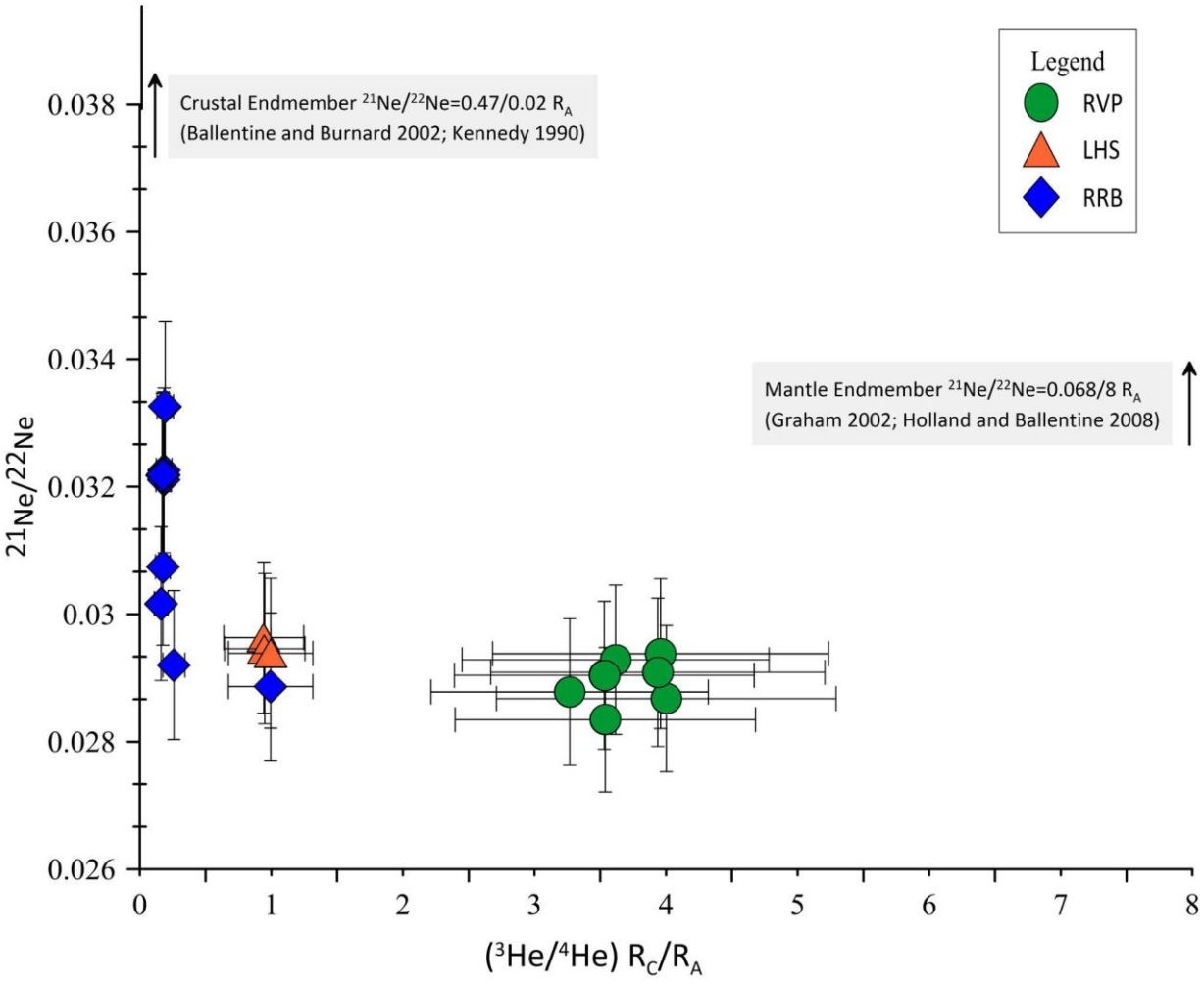

**Figure 5.** $^{21}Ne/^{22}Ne$ versus He-isotopic ratio ($R_C/R_A$) for the seeps in RRB, LHS and RVP, showing a coupling of $^{21}Ne$ and radiogenic $^{4}He$. Mantle and crustal endmember values have been added for reference. Vertical and horizontal error bars in the data are calculated at the 1 sigma level. All data in this figure are from samples collected in Cu-tubes and analysed in the Oxford Noble Laboratory.

### *5.2.3 Argon isotopes*

Argon is susceptible to atmospheric contributions, due to high Ar contents in the atmosphere, and therefore its measured concentration cannot be used directly to assess source contributions. However, by applying an air-correction to argon data, excess radiogenic argon ($^{40}Ar^*$) can be estimated using Eq. 2 (Graham, 2002).

$$^{40}Ar^* = (^{40}Ar/^{36}Ar_M - {}^{40}Ar/^{36}Ar_A) \times {}^{36}Ar_M \qquad (2)$$

where $^{36}Ar_M$ and $(^{40}Ar/^{36}Ar)_M$ are the measured $^{36}Ar$ abundance and argon isotopic ratios, respectively, and $(^{40}Ar/^{36}Ar)_A$ is the well-constrained air-ratio (298.6, Lee et al., 2006).

Using this equation, we calculate that for the RRB seeps, 51% to 65% of the Ar is radiogenic , the LHS seeps have 2.6% to 19% $^{40}Ar^*$ contributions and the RVP seeps have between 0.89% and 19% $^{40}Ar^*$ contributions. This is consistent with the observed trends between distance, He concentrations, $N_2$ concentrations and helium isotopic compositions (Supplementary Figure 4). The calculated $^{40}Ar^*$, from Eq. (2), can then be combined with measured $^{4}He$ to yield a $^{4}He/^{40}Ar^*$, which can offer insight into the sources of volatiles in each region as well as the overall degassing and fractionation history of the system. Gas seeps in RRB have an excess of radiogenic $^{4}He$, $^{40}Ar^*$ and $^{21}Ne^*$ (calculated analogously to $^{40}Ar^*$), which decrease systematically towards LHS and RVP (Figure 6; section 5.3.1), suggesting two-component mixing between crustal and mantle endmembers, which is ultimately a function of proximity to the volcanic center.

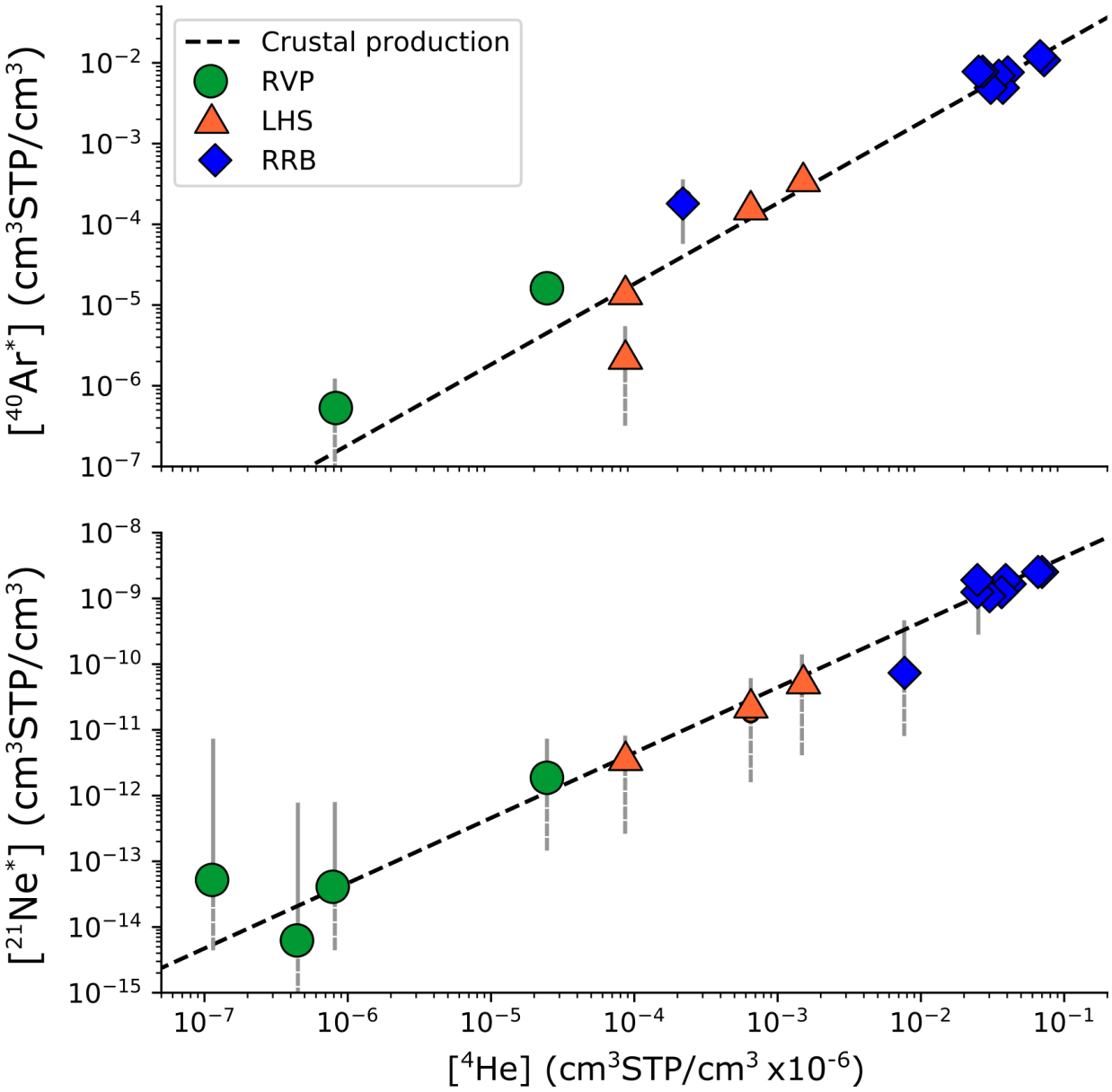


**Figure 6**. Radiogenic isotope abundances, alongside lines representing expected production for typical continental crust. Crustal production lines are $^{4}He/^{40}Ar = 5.5$ and $^{4}He/^{21}Ne = 2.7 \times 10^{7}$ (Ballentine & Burnard, 2002). $^{40}Ar^{*}$ is calculated following Eq. 2 and $^{21}Ne^{*}$ is calculated analogously. Dashed grey error bars indicate the unconstrained lower bound due to overlap between radiogenic isotope ratios and atmospheric values, within error. All data were determined in the Oxford Noble Laboratory using static mass spectrometry techniques.

### 5.3 The role of groundwater in regional subsurface gas migration

This section focuses on determining the accumulation, release and transport of deep crustal gases to the near surface. Conceptually, regional deep gas migration could occur through two mechanisms: 1) buoyant gas moving through a static water body, or 2) as dissolved gas within a migrating water phase. We use the air-derived noble gas (ANG's: $^{20}Ne$, $^{36}Ar$, $^{84}Kr$, $^{130}Xe$) isotopes to identify this relationship in gas seep samples and by mass balance (i.e., observed flux estimates), determine the role of groundwater in the regional deep gas migration process.

The mechanisms controlling the abundance of ANG's in groundwater, and their distribution between groundwater and other subsurface phases are well-studied (e.g., Zartman et al., 1961, Bosch and Mazor, 1988, Zaikowski and Spangler, 1990, Ballentine et al., 1991; 1996, Hiyagon and Kennedy, 1992, Pinti and Marty, 1995, Torgersen and Kennedy, 1999, Kipfer et al., 2002; Zhou et al., 2005; 2012, Gilfillan et al., 2008; 2009, Hunt et al., 2012, Aeschbach-Hertig and Solomon, 2013, Darrah et al., 2015; Barry et al., 2016, 2017, 2018, Tyne et al., 2021). The ANG's can therefore be used as proxies for the proportional volume of groundwater that a given gas sample has interacted with. Consideration of the bulk gas composition in turn enables the depth at which the gas phase would be fully dissolved within the groundwater to be calculated. When considered within the context of the sample setting, this determines whether the gas was dominantly transported as a gas phase or dissolved in solution (e.g., Ballentine et al., 1991; Ballentine and O'Nions, 1993, Ballentine and Sherwood Lollar, 2002; Barry et al., 2016).

When gas and groundwater phases interact in the subsurface, ANG's preferentially partition into the gas phase due to their low solubility in liquid, and therefore the concentration and elemental ratios of ANGs in the gas phase can provide insights into volumes of groundwater associated with their migration to the surface (Ballentine et al., 2002). This volumetric gas to water ratio ($V_g/V_w$) can be calculated using the following equation (3), after Byrne et al., (2020).

$$\frac{V_g}{V_w} = \frac{\rho_w C_i^{asw}}{C_i^{sample}} - \frac{16 T \rho_w}{195 \gamma_i K_i^m} \quad (3)$$

where $C_i^{asw}$ and $C_i^{sample}$ represent the abundances of a noble gas species *i* in the initial ASW and the sample respectively. $K_i^m$ is the Henry's constant (in units of atm kg $mol^{-1}$) which describes the solubility and partitioning between gas-water phases, and $\gamma_i$ is the Setschenow constant which accounts for non-ideality resulting from salinity. $\rho_w$ is the density of water (Fernandez-Prini et al., 2003).

$V_g/V_w$ values are conventionally calculated using only $^{20}Ne$ or $^{36}Ar$, as sedimentary rocks can contain significant amounts of excess adsorbed Kr and Xe (Podosek et al., 1981). We calculate $V_g/V_w$ values for our samples assuming an initial ASW composition equilibrated at the average Tanzanian surface-temperature of 295.5 K and zero salinity. Henry's Constants for partitioning were calculated for these conditions following Fernandez-Prini et al., (2003). Notably, if non-zero salinity or slightly different temperatures (i.e., within the expected recharge range) are used, it does not significantly affect our results or the subsequent discussion. Independent estimates for both $^{20}Ne$ and $^{36}Ar$ are in close agreement (Table 3), indicating there is no significant fractionation in the system. For the following discussion we use the $V_g/V_w$ values calculated using $^{36}Ar$.

$V_g/V_w$ values vary significantly with sample location; RRB samples have low $V_g/V_w$ below 0.1 (Table 5), whilst LHS samples are from 0.1 to 10, and RVP samples range from 3.0 to 12, indicating a much greater involvement of groundwater in the RRB compared to LHS and RVP. This could be due to greater volumes of groundwater present in the subsurface in the RRB locations, due to higher porosity or faster flux of groundwater through the area. However, a greater migration distance for the gas phase is likely required to explain such a large discrepancy across the region, as the gas phase will encounter larger volumes of groundwater during a longer migration path through the crust. Another possibility is that all ANG's are sourced by gas that includes some mantle-derivation, but the samples from RBB have a wider "spring shed", funneling water and gas from a broad section of crust due to tectonics and hydrology. In contrast, the mantle-derived RVP is dominated by vertical flux of gas associated with the volcanic region and with less capture of regional gas. In both scenarios, these findings are consistent with the high observed radiogenic $^4He$ contents in seeps, which also suggest extensive interaction with groundwater in order to concentrate the $^4He$.

### 1. 5.3.1 *Migration distance estimations*

Low $V_g/V_w$ is correlated with high radiogenic noble gas concentrations (Figure 7). This is strong evidence that there is a common mechanism controlling the abundance of both radiogenic and atmospheric noble gases in these samples. As noted above, greater migration distances are likely a key factor in producing low $V_g/V_w$ values, and it is probable that greater migration distances also lead to a greater entrainment of radiogenic isotopes from the crust (Figure 7). As a result, migration distance in the subsurface could be a key factor in concentrating He, and ultimately responsible for the high He abundances observed in the area.

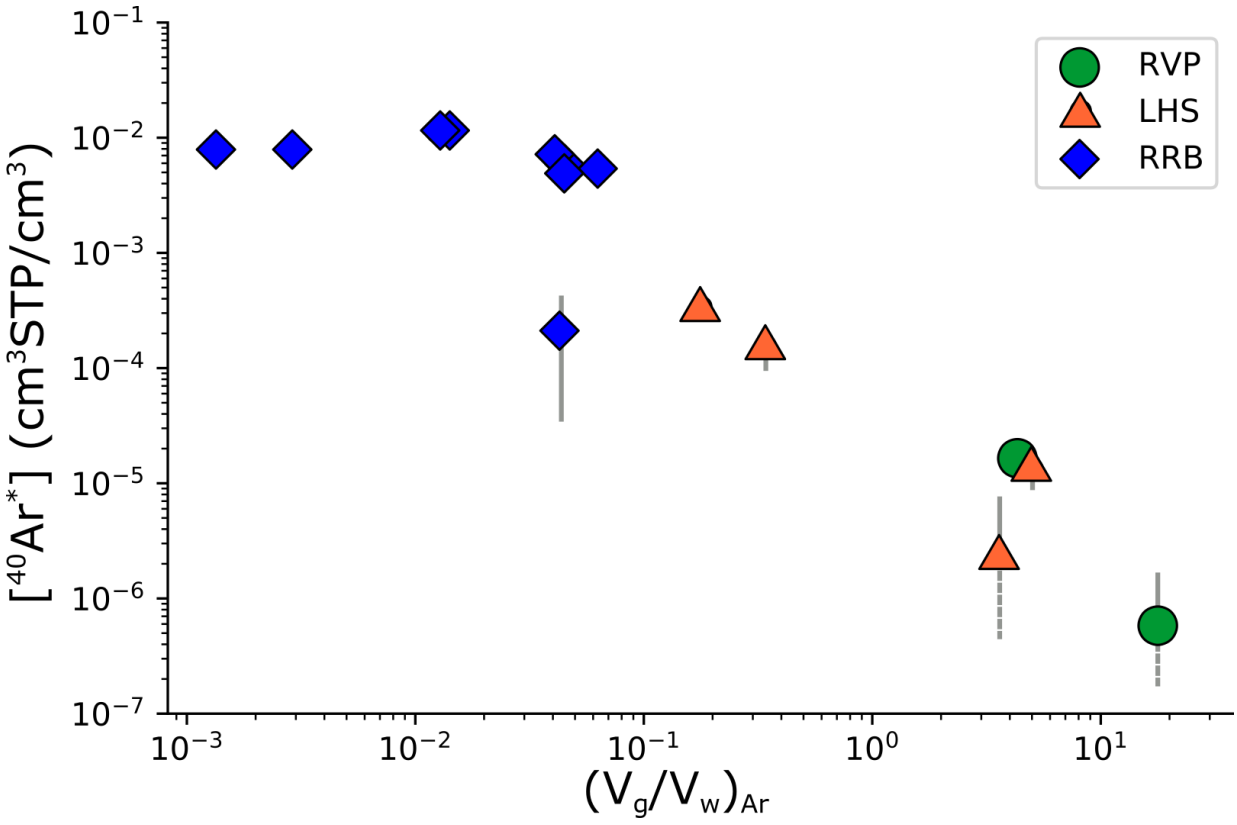


**Figure 7.** - Plot of $V_g/V_w$ (calculated using $^{36}Ar$) against radiogenic $^{40}Ar$. Dashed error bars (1-sigma) indicate unconstrained lower bound due to overlap between radiogenic isotope ratio and atmospheric value within error. Ar data in this figure were analyzed from Cu-tube samples in the Noble Laboratory.

The RVP region shows the highest $V_g/V_w$ values and therefore is inferred to have the shortest migration distances. This is perhaps unsurprising as the RVP is the most active volcanic center in the region in terms of both its degassing and geothermal behavior (Fontijn et al., 2010). The depth of the geothermal reservoir beneath RVP has in fact been estimated at around 380m (Alexander et al., 2016). This can be thought to represent a minimum migration distance for the

RVP and also a reasonable estimate of the order of magnitude of the true migration distance. The $V_g/V_w$ estimates suggest that LHS gases have interacted with on average ~18 times more water than RVP gases. Likewise, RRB gases have interacted with ~203 times more water than RVP gases. Using our independent migration distance estimate for RVP, we can simply scale according to the $V_g/V_w$ of the other regions in order to estimate their migration distances. In this way we estimate that LHS gases have migrated ~7 km and that RBB gases have migrated ~77 km. This is an approximate calculation but it is reasonably well aligned with the geographic distance between the two regions and RVP (Figure 1).

We therefore propose a simple conceptual migration model whereby the magmatic gases surfacing at RRB and LHS may have originated further southwards towards RVP, and that their migration likely included a significant lateral component in the subsurface (Figure 8). Similar migration patterns have been previously observed in related volcanic systems, including at Yellowstone National Park (Kharaka et al., 2000). Here, this increased migration is clearly correlated with increased $^4$He abundances, and as such, this observation gives an insight into the likely location of high He gases in similar systems.

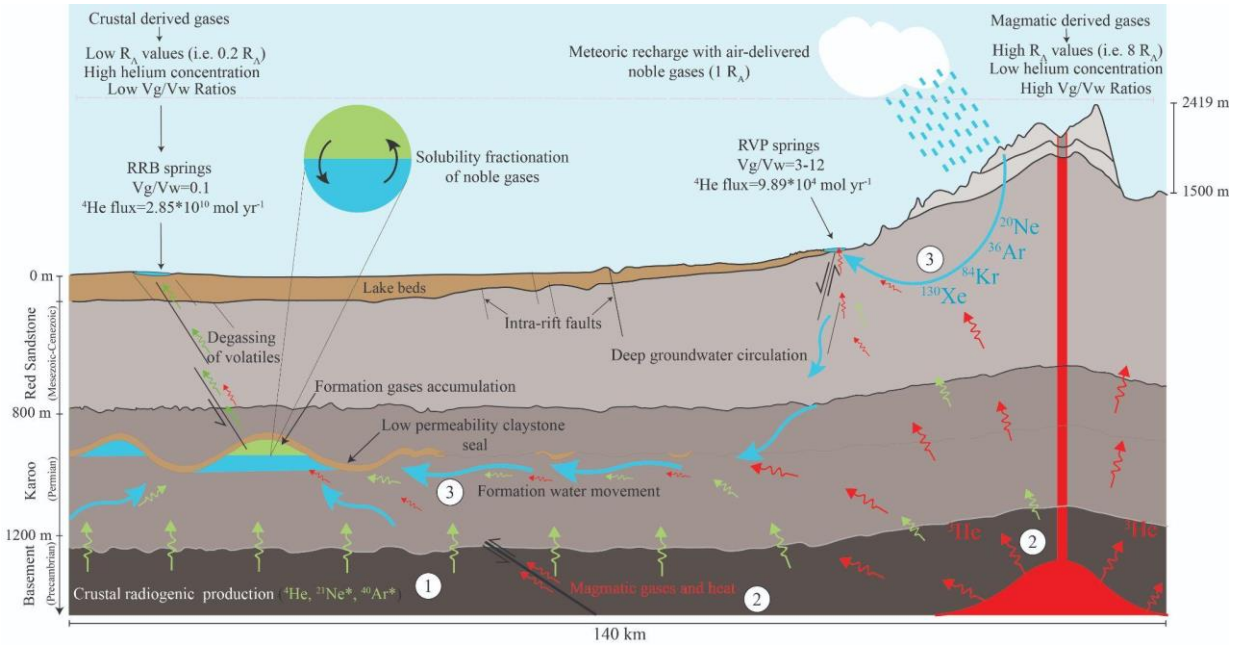


Figure 8. A schematic conceptual model illustrating the three stages of gas generation, accumulation and migration across the crustal surface. Stage 1: Crustal production of radiogenic ($^4$He and $^{40}$Ar) gases from the crust by decay of radioelements (i.e., $^{235,238}$U,$^{232}$Th and $^{40}$K and nucleogenic ($^{21}$Ne) production due to alpha reactions. Stage 2: Injection of mantle components in variable extents, controlled by distance to volcanic center, which invariably is associated with elevated heat, facilitating thermal release of radiogenic components in the crust's mineral

matrixes. Stage 3: Interaction of groundwater with the radiogenic produced gases. This stage overlaps with stage 2, as long durations of hydrodynamics are required in both primary migration (release from mineral) and in secondary migration (movement to traps) of gases to the accumulation zones. Faults and (thermal) magmatism provide mobilisation mechanisms of deep fluid circulation and focusing flow to the near surface as macroseeps/springs. The schematic conceptual model has been modified from Byrne et al., 2017.

### 2. *5.3.2. Degassing of radiogenic components*

Excess radiogenic and nucleogenic noble gases ($^{4}He$, $^{21}Ne^{*}$ and $^{40}Ar^{*}$) in the sampled gas seeps within RRB, RVP, and LHS indicate a preferential enrichment from the underlying basement rock (i.e., Mbozi Block rocks) (Ballentine and Sherwood Lollar, 2002). We note the average $^{4}He/^{40}Ar^{*}$ in RRB is ~4.7, which is close to the expected crustal value of 5±1 (Figure 6; Taylor and McLennan, 1985; Ballentine and Burnard, 2002). Three out of four gas seeps in LHS have an average $^{4}He/^{40}Ar^{*}$=5.0 with one outlier having a $^{4}He/^{40}Ar^{*}$ of 38.5. While the source of the high value is unclear, we surmise that it could be explained by different closure temperatures ($T_C$) between Ar ($T_C$=320-520 °C) and He ($T_C$=75-180 °C) leading to thermal fractionation and decreased release for argon (Blanckenburg et al., 1989; Ballentine et al., 1994; Reiners, 2005). This could be attributed to the accelerated cooling of the system across the Lupa Border fault or a shallow crustal source at the edge of the Tanzania craton (Elliot et al., 1993). Seeps in RVP shows an average $^{4}He/^{40}Ar^{*}$ of 1.9, consistent with degassed mantle gases (Kimani et al., 2021).

### 3. *5.3.3. He flux and crustal production ratio*

Radiogenic helium continuously produced within continental crust due to the decay of U and Th. In most tectonic environments, He is produced under steady state conditions (Torgersen and Clarke, 1985; Torgersen, 1989; Ballentine and Burnard, 2002) and continuously released to the atmosphere as it is produced. However, higher $^{4}He$ fluxes have been observed in some regions, attributed to either 1) abrupt tectonic-release of deeply-stored He, or 2) by enhanced advection of groundwater, thus mobilising, transporting and concentrating crustal gases that were generated over billions of years (Torgersen and Ivey, 1985; Lowenstern et al., 2014). This concentrated accumulation and mobilisation of He is a potential mechanism for commercially viable helium reservoirs to form. By constraining the relative rate of helium degassing in our study area, we can estimate the timescales of accumulation and volumes of crust required to explain the observed concentrations. In the following section, we show that our study area is characterised by excess crustal $^{4}He$ flux that cannot be explained by steady state $^{4}He$ generation in the

southwestern Tanzania crustal section (Ballentine and Burnard, 2002; Lowenstern et al., 2014). We quantify this excess, first by calculating the theoretical whole-crust (WC) $^4$He production rate (Eq. 4) using physical crustal parameters (i.e., crustal mass and radioelement concentration). Next, we combine previously published $CO_2$ fluxes from the EARS (Lee et al., 2016) with our measured $CO_2/^4$He ratios, which allows us to calculate $^4$He fluxes using the methods of Lowenstern et al., (2014). Finally, we relate excess $^4$He fluxes with our calculated volumetric gas/water ratios ($V_g/V_w$; section 5.3) in an attempt to explain the source of excess $^4$He in southwestern Tanzania.

The $^4$He production rate is well constrained as a function of the concentration of parent isotopes $^{235,238}$U and $^{232}$Th within the crust (after Ballentine & Burnard, 2002).

$$J_{4He} = (3.115 \times 10^6 + 1.272 \times 10^5)[U] + 7.710 \times 10^5[Th] \quad (4)$$

where $J_{4He}$ is the radiogenic $^4$He production in atoms g$^{-1}$ yr$^{-1}$, *[U]* and *[Th]* are the assumed average crustal compositions of U (2 ppm) and Th (10.7 ppm) respectively (Chaki et al, 2008). Using this equation, we calculate a $^4$He crustal production rate of $1.73 \times 10^7$ atoms g$^{-1}$ yr$^{-1}$. We can scale up to the entire crust of the region by multiplying by the total crustal mass of the region of interest.

$$Q^C_{4He} = (M_Y/N_A)\, J_{4He} \quad (5)$$

Where $Q^C_{4He}$ is the total crustal $^4$He flux in mol yr$^{-1}$, $M_Y$ is the mass of the crust in the region, and $N_A$ is Avogadro's constant. The entire region of southwestern Tanzania considered here has a surface area of ~14,000 km$^2$ and an average crustal thickness of ~37.5 km (Kim et al., 2009), giving a total mass of ~$1.57 \times 10^{21}$ g. Combining with the previous equation we can calculate a total $^4$He generation in the southwestern Tanzania region of 4.53 x $10^4$ mol yr$^{-1}$. We define this value as equivalent to one WC of $^4$He generation for comparison with our study areas.

The measured $^4$He/$CO_2$ ratios and published literature estimates of $CO_2$ degassing flux in the EARS were used to estimate a $^4$He degassing flux. Estimates of regional $CO_2$ degassing flux within the literature are variable, and depend on several assumptions used in their calculation as well as the particular regions studied. Lee et al., 2016 calculated the $CO_2$ degassing flux in the Magadi-Natron basin of Northern Tanzania to be $9.38 \times 10^7$ mol km$^{-2}$ yr$^{-1}$. However, Barry et al., 2013 reported a significantly lower total mantle-derived $CO_2$ flux of ~ $8.3 \times 10^4$ mol km$^{-2}$ yr$^{-1}$ in RVP. Both of these could be considered reasonable estimates for the region under consideration here, and we consider both in our following calculations to derive a range of estimates. Using

these literature values and under the assumption that they are comparable to our study area, we can calculate the degassing flux of $^4He$ using our measured $^4He/CO_2$ ratios:

$$Q^{meas}_{4He} = Q_{CO2} \times (^4He/CO_2)_{meas} \times f_{crustal} \quad (6)$$

where $Q_{CO2}$ is the $CO_2$ flux, $(^4He/CO_2)$ is the average measured $^4He/CO_2$ from our samples in each region and $f_{crustal}$ is the fraction of the sample $^4He$ derived from crustal sources. $f_{crustal}$ was calculated using an assumed mantle endmember of either 8 or 15 $R_A$ (i.e., depleted MORB or Plume) to derive a range of possible estimates.

Using the higher Lee et al., 2016 values for $CO_2$ flux, in the RRB we calculate a $^4He$ degassing flux of $1.97 \times 10^7$ mol $km^{-2}$ $yr^{-1}$ and a total degassing flux across the region of $2.85 \times 10^{10}$ mol $yr^{-1}$ (assuming a surface area of 2,248 $km^2$). This is five orders of magnitude larger than the crustal production rate for the entire southwestern Tanzania region, equivalent to ~$6.2 \times 10^5$ WC. Such a large $^4He$ flux cannot be accounted for by steady state degassing of $^4He$ over a geological time scale. Similarly, we estimate degassing fluxes for the LHS (380 $km^2$) and RVP (459 $km^2$) of ~100 WC and ~1.9 WC respectively. In terms of whole crust production, the RRB flux is significantly greater than the predicted He flux (~$1.5 \times 10^3$ WC) at Yellowstone (Lowenstern et al., 2014).

Following the same procedure presented above, we combine the Barry et al. (2013) RVP $CO_2$ flux estimates with our measured $^4He/CO_2$ in order to constrain the lower bound $CO_2$ flux. In RRB we calculated the $^4He$ degassing flux of $1.75 \times 10^4$ mol $km^{-2}$ $yr^{-1}$ and a total degassing flux of the entire region as $2.5 \times 10^7$ mol $yr^{-1}$ (assuming a surface area of 2,248 $km^2$). Even by adopting lower $CO_2$ flux estimates from Barry et al. (2013), the crustal production rate for $^4He$ in the RRB is still quite large, equivalent to ~$5.5 \times 10^3$ WC. Comparably, the LHS (380 $km^2$) and RVP (459 $km^2$) have estimated fluxes of ~$8.7 \times 10^{-2}$ WC and $1.7 \times 10^{-3}$ WC, respectively. These results clearly demonstrate that the RRB $^4He$ degassing flux is far from equilibrium, whilst the LHS and RVP may be closer or even below equilibrium degassing flux depending on the input assumptions.

The continuous tectonism in the rift from ~8.6 Ma to present (Ebinger, 1984) could account for the rapid release of $^4He$, especially in the RRB region, generated over billions of years, and accumulated in a short period after the inception of the rift. Furthermore, the documented long migration pathways (i.e., $V_g/V_w$; section 5.3), implies a basin-scale hydrogeological system in which involvement of groundwater plays a role in the enhanced fluid/gas accumulation, release

and transport of crustal $^{4}He$ in these hydrothermal systems. Areas such as RRB, which have extremely high crustal $^{4}He$ flux experienced a long migration pathway (section 5.3), while in LHS and RVP, the $^{4}He$ flux is lower, consistent with less groundwater involvement ($V_g/V_w$) across the region (Table 3; Table 4). This provides further evidence that groundwater migration plays a key role in degassing and concentration of large volumes of $^{4}He$.

## 2. 5.4 A conceptual model for He generation

The origin of high helium seeps at the RRB and LHS can be explained using a three-stage conceptual model, which interprets geochemical data within the context of the tectonic regime of the seeps.

Stage 1: production of radiogenic ($^{4}He$, $^{40}Ar$ and $^{21}Ne$) gases from the crust by decay of radioelements or nucleogenic production. Gas seeps found in regions with older thick basement rock tend to have lower He isotope ratios ($^{3}He/^{4}He$) and higher $^{4}He$ concentrations (Figure 3; Supplementary Figure 1a). In the context of helium accumulation, we can define the "source rock" as the old crustal craton which has been radiogenically producing $^{4}He$ over time. Within this conceptual framework, the older the source rock (in this case the Mbozi Block (~2.1Ga)) the higher the concentration of these radiogenic nuclides. In areas proximal to volcanic settings such as RVP, the accumulation of $^{4}He$ is diluted by addition of mantle components, (i.e., $^{3}He$ and $CO_2$ (Supplementary Figure 1c)).

Stage 2: Injection of mantle components to variable extent, controlled by distance to volcanic center, which invariably is associated with elevated heat, facilitating thermal release of radiogenic components trapped within the crust's mineral matrices. The EARS is actively undergoing rifting, which is linked to thinning of the lithosphere, rising of the asthenosphere and elevated thermal kinetic energy, which in turn provide a means of liberating radiogenic $^{4}He$ that has remained in mineral lattices (Chorowicz, 2005; Ebinger 2005; Pik et al., 2006; Danabalan, 2017).

Stage 3: Interaction of groundwater with the liberated radiogenic gases. This stage overlaps with stage 2, as long term hydrogeological cycles are required for basin-scale migration to occur. Our data show that the highest concentrations of helium are found in areas with the lowest gas to

water volume ratio ($V_g/V_w$) (Section 5.2.2), which are inferred from their high air-derived noble gas ($^{20}Ne$, $^{36}Ar$) concentrations in these samples. In section 5.3.3, we further constrain these areas (RRB) to have high crustal $^4He$ flux ($Q^C_{He}$) with an upper limit up to $6.2 \times 10^5$ WC, which decreases systematically moving from LHS (~100 WC) to RVP (~1.9 WC). These observations suggest a longer migration distance in the RRB compared to the LHS and RVP, as well as a relatively more rapid degassing of trapped $^4He$.

Nearly all seeps in this study are associated with fault systems, suggesting that subsurface structure exerts a significant control over volatile migration. Owing to extensional structure features in the RRB, $^4He$ sourced from different depths is "funneled" via the rift fault to structural traps, providing an explanation for the longer migration distance estimates as discussed in section 5.2.3. In summary, such a three-stage model can be employed in areas of high-helium accumulation, with ancient crustal basement rocks, sedimentary trapping structures and evidence for elevated heat flow and deep fault structures.

## 6. Conclusions

Here we report bulk gas (He-Ne-$N_2$-Ar-$CO_2$) and noble gas isotope data from three regions: 1) Rukwa Rift Basin, 2) Lupa Hydrothermal system, and 3) Rungwe Volcanic Province in southwestern Tanzania. These data offer insight into volatile sources, movements and processes (e.g., groundwater-volatile interaction, the influence of rifting on volatile distribution).

He-Ne-Ar-$N_2$-$CO_2$ seep composition can be explained by binary mixing between crustal and mantle endmembers, with distinct $^4$He-$^{21}$Ne*-$^{40}$Ar* coupled isotopic ratios across the study area. The lowest $^3$He/$^4$He (crustal-like signatures) correlate with high $^4$He concentration (i.e., RRB and LHS). Seeps with higher $^3$He/$^4$He (mantle-like signature) have low $^4$He contents are associated with high $CO_2$ concentrations, whilst He rich seeps are strongly associated with $N_2$, possibly related to low-temperature metamorphism of crustal rocks in the Mbozi block.

We use atmosphere-derived noble gases to calculate volumetric gas/water ratios from our samples, and we find there has been more groundwater interaction in the RRB than the LHS and RVP. This greater groundwater interaction is also associated with high $^4$He flux, orders of magnitude more than whole crust (WC) production rates.

Moreover, our results suggest a significant role for geological structures such as faults in focusing volatile manifestations in study areas. However, this is difficult to elucidate using only geochemical data, and should be the focus of future multidisciplinary studies. We note variable contribution and extent of mixing controlled by spatial location of seeps and their proximity to rift-related faults along with distance to volcanic center.

## 2. 7. Acknowledgements

We kindly acknowledge the sponsorship from Helium One Limited company funding this work. Specifically, we thank Tom Abraham-James and Josh Bluett for their steadfast support of this project. We also thank the Oxford Noble Lab for providing funding for the noble gas analyses.

## 3. References


Aeschbach-Hertig, W., Solomon, D.K., 2013. Noble Gas Thermometry in Groundwater Hydrology. pp. 81–122. https://doi.org/10.1007/978-3-642-28836-4_5

Alexander, K., W. B. Cumming, and Marini., L 2006. Technical review of geothermal potential of Kibiro geothermal prospect, Uganda: Proceedings In 6th African Rift Geothermal Conference, Addis Ababa, Ethiopia, 2-4.

Aiuppa, A., Casetta, F., Coltorti, M., Stagno, V., Tamburello, G., 2021. Carbon concentration increases with depth of melting in Earth's upper mantle. Nature Geoscience. https://doi.org/10.1038/s41561-021-00797-y

Ballentine, C.J., Burgess, R., Marty, B., 2002. Tracing fluid origin, transport and interaction in the crust. Rev. Mineral. Geochemistry 47. https://doi.org/10.2138/rmg.2002.47.13

Ballentine, C.J., Burnard, P.G., 2002. Production, Release and Transport of Noble Gases in the Continental Crust. Rev. Mineral. Geochemistry 47, 481–538. https://doi.org/10.2138/rmg.2002.47.12

Ballentine, C.J., Holland, G., 2008. What $CO_2$ well gases tell us about the origin of noble gases in the mantle and their relationship to the atmosphere. Philos. Trans. R. Soc. A Math. Phys. Eng. Sci. 366, 4183–4203. https://doi.org/10.1098/rsta.2008.0150

Ballentine, C.J., Mazurek, M., Gautschi, A., 1994. Thermal constraints on crustal rare gas release and migration: Evidence from Alpine fluid inclusions. Geochim. Cosmochim. Acta 58, 4333–4348. https://doi.org/10.1016/0016-7037(94)90337-9

Ballentine, C.J., O'Nions, R.K., 1993. The use of natural He, Ne and Ar isotopes as constraints on hydrocarbon transport. Geol. Soc. London, Pet. Geol. Conf. Ser. 4, 1339–1345. https://doi.org/10.1144/0041339

Ballentine, C.J., O'Nions, R.K., Coleman, M.L., 1996. A Magnus opus: Helium, neon, and argon isotopes in a North Sea oilfield. Geochim. Cosmochim. Acta 60, 831–849. https://doi.org/10.1016/0016-7037(95)00439-4

Ballentine, C.J., O'Nions, R.K., Oxburgh, E.R., Horvath, F., Deak, J., 1991. Rare gas constraints on hydrocarbon accumulation, crustal degassing and groundwater flow in the Pannonian Basin. Earth Planet. Sci. Lett. 105, 229–246. https://doi.org/10.1016/0012-821X(91)90133-3

Ballentine, C.J., Sherwood Lollar, B., 2002. Regional groundwater focusing on nitrogen and noble gases into the Hugoton-Panhandle giant gas field, USA. Geochim. Cosmochim. Acta 66, 2483–2497. https://doi.org/10.1016/S0016-7037(02)00850-5

Barry, P.H., Hilton, D.R., Fischer, T.P., de Moor, J.M., Mangasini, F., Ramirez, C., 2013. Helium and carbon isotope systematics of cold "mazuku" $CO_2$ vents and hydrothermal gases and fluids from Rungwe Volcanic Province, southern Tanzania. Chem. Geol. 339, 141–156. https://doi.org/10.1016/j.chemgeo.2012.07.003

Barry, P.H., Kulongoski, J.T., Landon, M.K., Tyne, R.L., Gillespie, J.M., Stephens, M.J., Hillegonds, D.J., Byrne, D.J., Ballentine, C.J., 2018. Tracing enhanced oil recovery signatures in casing gases from the Lost Hills oil field using noble gases. Earth Planet. Sci. Lett. 496, 57–67. https://doi.org/10.1016/j.epsl.2018.05.028

Barry, P.H., Lawson, M., Meurer, W.P., Danabalan, D., Byrne, D.J., Mabry, J.C., Ballentine, C.J., 2017. Determining fluid migration and isolation times in multiphase crustal domains using noble gases 1–4. https://doi.org/10.1130/G38900.1

Barry, P.H., Lawson, M., Meurer, W.P., Warr, O., Mabry, J.C., Byrne, D.J., Ballentine, C.J., 2016. ScienceDirect Noble gases solubility models of hydrocarbon charge mechanism in the Sleipner Vest gas field. Geochim. Cosmochim. Acta 194, 291–309. https://doi.org/10.1016/j.gca.2016.08.021

Barry, P. and Hilton, D.R., 2016. Release of subducted sedimentary nitrogen throughout Earth's mantle. *Geochemical Perspectives Letters*, *2*(2). https://doi.org/10.7185/geochemlet.1615

Barry, P.H., de Moor, J.M., Giovannelli, D. et al. Forearc carbon sink reduces long-term

volatile recycling into the mantle. Nature 568, 487–492 (2019). https://doi.org/10.1038/s41586-019-1131-5

Barry, P.H., Broadley, M.W., 2021. Nitrogen and noble gases reveal a complex history of metasomatism in the Siberian lithospheric mantle. Earth Planet. Sci. Lett. 556, 116707. https://doi.org/10.1016/J.EPSL.2020.116707

Bebout, G.E., Fogel, M.L., 1992. Nitrogen-isotope compositions of metasedimentary rocks in the Catalina Schist, California: Implications for metamorphic devolatilization history. Geochim. Cosmochim. Acta 56, 2839–2849. https://doi.org/10.1016/0016-7037(92)90363-N

Bekaert, D.V., Turner, S.J., Broadley, M.W., Barnes, J.D., Halldórsson, S.A., Labidi, J., Wade, J., Walowski, K.J. and Barry, P.H., 2020. Subduction-Driven Volatile Recycling: A Global Mass Balance. *Annual Review of Earth and Planetary Sciences*, *49*. https://doi.org/10.1146/annurev-earth-071620-055024

Blanckenburg, F.., Villa, I.M., Baur, H., Morteani, G., Steiger, R.H., 1989. Time calibration of a PT-path from the Western Tauern Window, Eastern Alps: the problem of closure temperatures. Contrib. to Mineral. Petrol. 101, 1–11. https://doi.org/10.1007/BF00387196

Boniface, N., Schenk, V., 2012. Neoproterozoic eclogites in the Paleoproterozoic Ubendian Belt of Tanzania: Evidence for a Pan-African suture between the Bangweulu Block and the Tanzania Craton. Precambrian Res. 208–211, 72–89. https://doi.org/10.1016/j.precamres.2012.03.014

Boniface, N., Schenk, V., Appel, P., 2012. Paleoproterozoic eclogites of MORB-type chemistry and three Proterozoic orogenic cycles in the Ubendian Belt (Tanzania): Evidence from monazite and zircon geochronology, and geochemistry. Precambrian Res. 192–195, 16–33. https://doi.org/10.1016/j.precamres.2011.10.007

Boniface, N., Tsujimori, T., 2019. Pillow lava basalts with back-arc MORB affinity from the Usagaran Belt, Tanzania: relics of Orosirian ophiolites. J. Geol. Soc. London. 176, 1007–1021. https://doi.org/10.1144/jgs2018-205

Bosch, A., Mazor, E., 1988. Natural gas association with water and oil as depicted by atmospheric noble gases: case studies from the southeastern Mediterranean Coastal Plain. Earth Planet. Sci. Lett. 87, 338–346. https://doi.org/10.1016/0012-821X(88)90021-0

Bräuer, K., Kämpf, H., Niedermann, S., Strauch, G., Weise, S.M., 2004. Evidence for a nitrogen flux directly derived from the European subcontinental mantle in the Western Eger Rift, Central Europe. Geochim. Cosmochim. Acta 68, 4935–4947. https://doi.org/10.1016/j.gca.2004.05.032

Brennwald, Matthias S, Schmidt, M., Oser, J., Kipfer, R., 2016. A Portable and Autonomous Mass Spectrometric System for On-Site Environmental Gas Analysis. https://doi.org/10.1021/acs.est.6b03669

Brennwald, Matthias S., Schmidt, M., Oser, J., Kipfer, R., 2016. A Portable and Autonomous Mass Spectrometric System for On-Site Environmental Gas Analysis. Environ. Sci. Technol. 50, 13455–13463. https://doi.org/10.1021/acs.est.6b03669

Broadley, M.W., Barry, P.H., Bekaert, D. V., Byrne, D.J., Caracausi, A., Ballentine, C.J., Marty, B., 2020. Identification of chondritic krypton and xenon in Yellowstone gases and the timing of terrestrial volatile accretion. Proc. Natl. Acad. Sci. 117, 13997–14004. https://doi.org/10.1073/pnas.2003907117

Brown, A.A., 2010. PS Formation of High Helium Gases : A Guide for Explorationists * i.

Broadley, M.W., Barry, P.H., Ballentine, C.J., Taylor, L.A., Burgess, R., 2018. End-Permian extinction amplified by plume-induced release of recycled lithospheric volatiles. Nat. Geosci. 11, 682–687. https://doi.org/10.1038/s41561-018-0215-4

Brune, S., Williams, S.E., Müller, R.D., 2017. Potential links between continental rifting, CO2 degassing and climate change through time. Nat. Geosci. 10, 941–946. https://doi.org/10.1038/s41561-017-0003-6

Burgess, R., Sumino, H., Teagle, D.A.H., 2016. ScienceDirect The contribution of hydrothermally altered ocean crust to the mantle halogen and noble gas cycles. Geochim.

Cosmochim. Acta 183, 106–124. https://doi.org/10.1016/j.gca.2016.03.014

Burnard, P., 1997. Vesicle-Specific Noble Gas Analyses of "Popping Rock": Implications for Primordial Noble Gases in Earth. Science (80-. ). 276, 568–571. https://doi.org/10.1126/science.276.5312.568

Byrne, D.J., Barry, P.H., Lawson, M., Ballentine, C.J., 2018. Noble gases in conventional and unconventional petroleum systems. Geol. Soc. Spec. Publ. 468, 127–149. https://doi.org/10.1144/SP468.5

Byrne, D.J., Barry, P.H., Lawson, M., Ballentine, C.J., 2020. The use of noble gas isotopes to constrain subsurface fluid flow and hydrocarbon migration in the East Texas Basin. Geochim. Cosmochim. Acta 268, 186–208. https://doi.org/10.1016/j.gca.2019.10.001

Camelbeeck, T., Iranga, M.D., 1996. Deep crustal earthquakes and active faults along the Rukwa trough, eastern Africa. Geophys. J. Int. 124, 612–630. https://doi.org/10.1111/j.1365-246X.1996.tb07040.x

Chorowicz, J., 2005a. The East African rift system. J. African Earth Sci. 43, 379–410. https://doi.org/10.1016/j.jafrearsci.2005.07.019

Chorowicz, J., Chorowicz, J., 2015. The East African rift system The East African rift system. https://doi.org/10.1016/j.jafrearsci.2005.07.019

Crabtree, D.C., Chesworth, W., 1992. Rift Related Magmatism and the Petrogenesis of Lavas from the Kiejo Eruptive, Rungwe Volcanic Province, S.W. Tanzania. Springer, Dordrecht, pp. 71–82. https://doi.org/10.1007/978-94-017-0833-3_6

Craddock, William H., Blondes, M.S., DeVera, C.A., Hunt, A.G., 2017. Mantle and crustal gases of the Colorado Plateau: Geochemistry, sources, and migration pathways. Geochim. Cosmochim. Acta 213, 346–374. https://doi.org/10.1016/j.gca.2017.05.017

Daly, M.C., 1988. Crustal shear zones in Central Africa: a kinematic approach to Proterozoic tectonics. Episodes 11, 5–11. https://doi.org/10.18814/epiiugs/1988/v11i1/003

Darrah, T.H., Jackson, R.B., Vengosh, A., Warner, N.R., Whyte, C.J., Walsh, T.B., Kondash, A.J., Poreda, R.J., 2015. The evolution of Devonian hydrocarbon gases in shallow aquifers of the northern Appalachian Basin: Insights from integrating noble gas and hydrocarbon geochemistry. Geochim. Cosmochim. Acta 170, 321–355. https://doi.org/10.1016/j.gca.2015.09.006

Danabalan, D., 2017. Helium : Exploration Methodology for a Strategic Resource. PhD thesis, Durham University.

Danabalan, D., Gluyas, J.G., Ballentine, C.J., 2017. Helium-Producing Fields, Global Resources, and Reserves.

Danabalan, D., Gluyas, J.G., Macpherson, C.G., Abraham-James, T.H., Bluett, J.J., Barry, P.H., Ballentine, C.J., 2016. New High-Grade Helium Discoveries in Tanzania. Goldschmidt Conf. 47, 2497.

Delalande, M., Bergonzini, L., Branchu, P., Filly, A., Williamson, D., 2008. Hydroclimatic and geothermal controls on the salinity of Mbaka Lakes (SW Tanzania): Limnological and paleolimnological implications. J. Hydrol. 359, 274–286. https://doi.org/10.1016/j.jhydrol.2008.07.007

Delalande, M., Bergonzini, L., Gherardi, F., Guidi, M., Andre, L., Abdallah, I., Williamson, D., 2011. Fluid geochemistry of natural manifestations from the Southern Poroto-Rungwe hydrothermal system (Tanzania): Preliminary conceptual model. J. Volcanol. Geotherm. Res. 199, 127–141. https://doi.org/10.1016/j.jvolgeores.2010.11.002

Delvaux, D., 2001. Karoo rifting in western Tanzania: precursor of Gondwana break-up ? Contrib. to Geol. Palaeontol. Gondwana honour Helmut Wopfner 111–125.

Delvaux, D., Kraml, M., Sierralta, M., Wittenberg, A., Mayalla, J.W., Kabaka, K., Makene, C., 2010a. Surface Exploration of a Viable Geothermal Resource in Mbeya area , SW Tanzania . Part I : Geology of the Ngozi – Songwe Geothermal System 25–29.

Delvaux, D., Kraml, M., Sierralta, M., Wittenberg, A., Mayalla, J.W., Kabaka, K., Makene, C., 2010b. Surface Exploration of a Viable Geothermal Resource in Mbeya area , SW Tanzania . Part I : Geology of the Ngozi – Songwe Geothermal System Surface Exploration of a Viable Geothermal Resource in Mbeya area , SW Tanzania . Part I : Geology of the Ngozi – So.

Delvaux, D., Temu, E.B., Deino, A., Kraml, M., 2013. Tectonic evolution of the Rukwa rift basin and interaction with the Rungwe Volcanic Province , Western Tanzania 2013.

De Waele, B., Johnson, S.P., Pisarevsky, S.A., 2008. Palaeoproterozoic to Neoproterozoic growth and evolution of the eastern Congo Craton: Its role in the Rodinia puzzle. Precambrian Res. 160, 127–141. https://doi.org/10.1016/j.precamres.2007.04.020

Dunai, T.J., Porcelli, D., 2002. Storage and Transport of Noble Gases in the Subcontinental Lithosphere. Rev. Mineral. Geochemistry 47, 371–409. https://doi.org/10.2138/rmg.2002.47.10

Eberhardt, P., Eugster, O., Marti, K., 1965. Notizen: A Redetermination of the Isotopic Composition of Atmospheric Neon. Zeitschrift für Naturforsch. A 20, 623–624. https://doi.org/10.1515/zna-1965-0420

Ebinger, C.J., 1989. Tectonic development of the western branch of the East African rift system Tectonic development of the western branch of the East African rift system 885–903. https://doi.org/10.1130/0016-7606(1989)101

Ebinger, C., 2005. Continental break-up: The East African perspective. Astron. Geophys. 46, 2.16-2.21. https://doi.org/10.1111/j.1468-4004.2005.46216.x

Elliot, T., Ballentine, C.J., O'Nions, R.K., Ricchiuto, T., 1993. Carbon, helium, neon and argon isotopes in a Po basin (northern Italy) natural gas field. Chem. Geol. 106, 429–440. https://doi.org/10.1016/0009-2541(93)90042-H

Farley, K. A., Natland, J. H., & Craig, H. (1992). Binary mixing of enriched and undegassed (primitive?) mantle components (He, Sr, Nd, Pb) in Samoan lavas. *Earth and Planetary Science Letters*, *111*(1), 183-199.

Fernández-Prini, R., Alvarez, J.L., Harvey, A.H., 2003. Henry's Constants and Vapor–Liquid Distribution Constants for Gaseous Solutes in H2O and D2O at High Temperatures. Journal of Physical and Chemical Reference Data 32, 903–916. https://doi.org/10.1063/1.1564818

Fischer, T.P., Giggenbach, W.F., Sano, Y., Williams, S.N., 1998. Fluxes and sources of volatiles discharged from Kudryavy, a subduction zone volcano, Kurile Islands. Earth Planet. Sci. Lett. 160, 81–96. https://doi.org/10.1016/S0012-821X(98)00086-7

Fischer, T.P., Takahata, N., Sano, Y., Sumino, H., Hilton, D.R., 2005. Nitrogen isotopes of the mantle: Insights from mineral separates. Geophys. Res. Lett. 32, L11305. https://doi.org/10.1029/2005GL022792

Fischer, T.P., Burnard, P., Marty, B., Hilton, D.R., Füri, E., Palhol, F., Sharp, Z.D., Mangasini, F., 2009. Upper-mantle volatile chemistry at Oldoinyo Lengai volcano and the origin of carbonatites. Nature 459, 77–80. https://doi.org/10.1038/nature07977

Foley, S.F., Fischer, T.P., 2017.An essential role for continental rifts and lithosphere in the deep carbon cycle. NatureGeosci 10, 897–902.h017.An essential role for continental rifts and lithosphere in the deep carbon cycle. NatureGeosci 10, 897–902.h

Fontijn, K., Ernst, G.G.J., Elburg, M.A., Williamson, D., Abdallah, E., Kwelwa, S., Mbede, E., Jacobs, P., 2010. Holocene explosive eruptions in the Rungwe Volcanic Province , Tanzania. J. Volcanol. Geotherm. Res. 196, 91–110. https://doi.org/10.1016/j.jvolgeores.2010.07.021

Fontijn, K., Williamson, D., Mbede, E., Ernst, G.G.J., 2012. Journal of African Earth Sciences The Rungwe Volcanic Province , Tanzania – A volcanological review. J. African Earth Sci. 63, 12–31. https://doi.org/10.1016/j.jafrearsci.2011.11.005

Füri, E., Hilton, D.R., Halldórsson, S.A., Barry, P.H., Hahm, D., Fischer, T.P., Grönvold, K., 2010. Apparent decoupling of the He and Ne isotope systematics of the Icelandic mantle: The role of He depletion, melt mixing, degassing fractionation and air interaction. Geochim. Cosmochim. Acta 74, 3307–3332. https://doi.org/10.1016/j.gca.2010.03.023

Furman, T., Bryce, J.G., Karson, J., Iotti, A., 2004. East African Rift System (EARS) Plume

Structure: Insights from Quaternary Mafic Lavas of Turkana, Kenya. J. Petrol. 45, 1069–1088. https://doi.org/10.1093/petrology/egh004

Gautheron, C., Moreira, M., 2002. Helium signature of the subcontinental lithospheric mantle. Earth Planet. Sci. Lett. 199, 39–47. https://doi.org/10.1016/S0012-821X(02)00563-0

Giggenbach, W.F., 1992. Isotopic shifts in waters from geothermal and volcanic systems along convergent plate boundaries and their origin. Earth Planet. Sci. Lett. 113, 495–510. https://doi.org/10.1016/0012-821X(92)90127-H

Giggenbach, W.F., 1996. Chemical Composition of Volcanic Gases, in: Monitoring and Mitigation of Volcano Hazards. Springer Berlin Heidelberg, Berlin, Heidelberg, pp. 221–256. https://doi.org/10.1007/978-3-642-80087-0_7

Gilfillan, S.M.V., Ballentine, C.J., 2018. He, Ne and Ar 'snapshot' of the subcontinental lithospheric mantle from CO2 well gases. Chem. Geol. 480, 116–127. https://doi.org/10.1016/j.chemgeo.2017.09.028

Gilfillan, S.M. V, Ballentine, C.J., Holland, G., Blagburn, D., Sherwood, B., Stevens, S., Schoell, M., Cassidy, M., 2008. The noble gas geochemistry of natural $CO_2$ gas reservoirs from the Colorado Plateau and Rocky Mountain provinces , USA 72, 1174–1198. https://doi.org/10.1016/j.gca.2007.10.009

Gilfillan, S.M. V, Lollar, B.S., Holland, G., Blagburn, D., Stevens, S., Schoell, M., Cassidy, M., Ding, Z., Zhou, Z., Lacrampe-couloume, G., Ballentine, C.J., No, B.B., No, M., 2009. Solubility trapping in formation water as dominant CO 2 sink in natural gas fields. Nature 458, 614–618. https://doi.org/10.1038/nature07852

Graham, D.W., 2002. Noble Gas Isotope Geochemistry of Mid-Ocean Ridge and Ocean Island Basalts: Characterization of Mantle Source Reservoirs. Rev. Mineral. Geochemistry 47, 247–317. https://doi.org/10.2138/rmg.2002.47.8

Grynia, E., Griffin, P.J., 2016. Helium in Natural Gas - Occurrence and Production. J. Nat. Gas Eng. 1, 163–215. https://doi.org/10.7569/JNGE.2016.692506

Halldórsson, S.A., Hilton, D.R., Scarsi, P., Abebe, T. and Hopp, J., 2014. A common mantle plume source beneath the entire East African Rift System revealed by coupled helium-neon systematics. *Geophysical Research Letters*, *41*(7), pp.2304-2311. https://doi.org/10.1002/2014GL059424

Harkin, D.A., 1960. The Rungwe Volcanics at the Northern End of Lake Nyasa.

Heilman, E., Kolawole, F., Atekwana, E.A., Mayle, M., 2018. Controls of basement fabric on rift coupling and development of normal fault geometries: Insights from the Rukwa -- North Malawi Rift. EarthArxiv. https://doi.org/10.31223/osf.io/akgr6

Hilton, D.R., Halldórsson, S.A., Barry, P.H., Fischer, T.P., Moor, J.M. De, Ramirez, C.J., Mangasini, F., Scarsi, P., 2011. Helium isotopes at Rungwe Volcanic Province , Tanzania , and the origin of East African Plateaux 38, 1–5. https://doi.org/10.1029/2011GL049589

Hilton D. R,. and Porcelli, D. "3.7 - Noble gases as mantle tracers," in Treatise on Geochemistry (Second Edition), vol. 3, pp. 293–325, 2014.

Hiyagon, H., Kennedy, B.., 1992. Noble gases in $CH_4$-rich gas fields, Alberta, Canada. Geochim. Cosmochim. Acta 56, 1569–1589. https://doi.org/10.1016/0016-7037(92)90226-9

Hochstein, M.P., Temu, E.P., Moshy, C.M.A., 2000. Geothermal Resources of Tanzania 1233–1238.

Hodgson, I., Illsley-Kemp, F., Gallacher, R.J., Keir, D., Ebinger, C.J., Mtelela, K., 2017. Crustal Structure at a Young Continental Rift: A Receiver Function Study From the Tanganyika Rift. Tectonics 36, 2806–2822. https://doi.org/10.1002/2017TC004477

Hunt, A.G., Darrah, T.H., Poreda, R.J., 2012. Determining the source and genetic fingerprint of natural gases using noble gas geochemistry: A northern Appalachian Basin case study. Am. Assoc. Pet. Geol. Bull. 96, 1785–1811. https://doi.org/10.1306/03161211093

Irwin, W.P., Barnes, I., 1980. Tectonic relations of carbon dioxide discharges and earthquakes. J. Geophys. Res. 85, 3115. https://doi.org/10.1029/JB085iB06p03115

James, T., 1967. Thermal springs in Tanzania. Inst. Min. Metall., Trans., Sect. B, 76:729

Jones, M.J., 1985. The weathered zone aquifers of the basement complex areas of Africa. Q. J. Eng. Geol. Hydrogeol. 18, 35–46. https://doi.org/10.1144/GSL.QJEG.1985.018.01.06

Kazimoto, E.O., Schenk, V., Appel, P., 2015. Granulite-facies metamorphic events in the northwestern Ubendian Belt of Tanzania: Implications for the Neoarchean to Paleoproterozoic crustal evolution. Precambrian Res. 256, 31–47. https://doi.org/10.1016/j.precamres.2014.10.016

Kazimoto, E.O., Schenk, V., Berndt, J., 2014. Neoarchean and Paleoproterozoic crust formation in the Ubendian Belt of Tanzania: Insights from zircon geochronology and geochemistry. Precambrian Res. 252, 119–144. https://doi.org/10.1016/j.precamres.2014.06.020

Kennedy, B.M., Hiyagon, H., Reynolds, J.H., 1990. Crustal neon: a striking uniformity. Earth Planet. Sci. Lett. 98, 277–286. https://doi.org/10.1016/0012-821X(90)90030-2

Kervyn, F., Ayub, S., Kajara, R., Kanza, E., Temu, B., 2006. Evidence of recent faulting in the Rukwa rift (West Tanzania) based on radar interferometric DEMs. J. African Earth Sci. 44, 151–168. https://doi.org/10.1016/j.jafrearsci.2005.10.008

Kharaka, Y.K., Sorey, M.L., Thordsen, J.J., 2000. Large-scale hydrothermal fluid discharges in the Norris–Mammoth corridor, Yellowstone National Park, USA. J. Geochemical Explorer. 69–70, 201–205. https://doi.org/10.1016/S0375-6742(00)00025-X

Kilembe, E.A., Rosendahl, B.R., 1992. Structure and stratigraphy of the Rukwa rift. Tectonophysics 209, 143–158. https://doi.org/10.1016/0040-1951(92)90016-Y

Kim, S., Nyblade, A.A., Baag, C.E., 2009. Crustal velocity structure of the Rukwa Rift in the western branch of the East African Rift System. South African J. Geol. 112, 251–260. https://doi.org/10.2113/gssajg.112.3-4.251

Kimani, C.N., Kasanzu, C.H., Tyne, R.L., Mtili, K.M., Byrne, D.J., Kazimoto, E.O., Hillegonds, D.J., Ballentine, C.J., Barry, P.H., *in review this issue*. He, Ne, Ar and $CO_2$ Systematics of the Rungwe Volcanic Province, Tanzania: Implications for Fluid Source and Dynamics. *Chemical Geology*.

King, D., Metcalfe, E., 2013. Rift Zones as a Case Study for Advancing Geothermal Occurence Models. Proc. Thirty-Eighth Work. Geothermal Reservoir Engineering. 11-13.

Kipfer, R., Aeschbach-Hertig, W., Peeters, F., Stute, M., 2002. Noble Gases in Lakes and Ground Waters. Rev. Mineral. Geochemistry 47, 615–700. https://doi.org/10.2138/rmg.2002.47.14

Kirschbaum, M.A., Lillis, P.G., Roberts, L.N.R., 2007. Geologic assessment of undiscovered oil and gas resources in the Phosphoria Total Petroleum System of the Wind River Basin Province, Wyoming. USGS Digit. Data Ser. DDS-69-J, 1–24. https://doi.org/10.3133/ds69J3

Kiyosu, Y., 1986. Variations in N2/Ar and He/Ar ratios of gases from some volcanic areas in Northeastern Japan. Geochem. J. 19, 275–281. https://doi.org/10.2343/geochemj.19.275

Kraml, M., Ochmann, N., Leible, D., Kling, T., Chiragwile, S.A., Jodocy, M., 2014. Results of the Pre-Feasibility Study on Ngozi Geothermal Project in Tanzania 1–10.

Lee, J.Y., Marti, K., Severinghaus, J.P., Kawamura, K., Yoo, H.S., Lee, J.B., Kim, J.S., 2006. A redetermination of the isotopic abundances of atmospheric Ar. Geochim. Cosmochim. Acta 70, 4507–4512. https://doi.org/10.1016/j.gca.2006.06.1563

Lee, H., Fischer, T.P., Muirhead, J.D., Ebinger, C.J., Kattenhorn, S.A., Sharp, Z.D., Kianji, G., Takahata, N., Sano, Y., 2017. Incipient rifting accompanied by the release of subcontinental lithospheric mantle volatiles in the Magadi and Natron basin, East Africa. J. Volcanol. Geotherm. Res. 346, 118–133. https://doi.org/10.1016/j.jvolgeores.2017.03.017

Lee, H., Muirhead, J.D., Fischer, T.P., Ebinger, C.J., Kattenhorn, S.A., Sharp, Z.D., Kianji, G., 2016. Massive and prolonged deep carbon emissions associated with continental rifting. Nat.

Geosci. 9, 145–149. https://doi.org/10.1038/ngeo2622

Lenoir, J.L., Liégeois, J.P., Theunissen, K., Klerkx, J., 1994. The Palaeoproterozoic Ubendian shear belt in Tanzania: geochronology and structure. J. African Earth Sci. 19, 169–184. https://doi.org/10.1016/0899-5362(94)90059-0

Lippmann-Pipke, J., Sherwood Lollar, B., Niedermann, S., Stroncik, N.A., Naumann, R., van Heerden, E., Onstott, T.C., 2011. Neon identifies two billion year old fluid component in Kaapvaal Craton. Chem. Geol. 283, 287–296. https://doi.org/10.1016/j.chemgeo.2011.01.028
Lowenstern, J.B., Evans, W.C., Bergfeld, D., Hunt, A.G., 2014. Prodigious degassing of a billion years of accumulated radiogenic helium at Yellowstone. Nature 506, 355–358. https://doi.org/10.1038/nature12992

Mamyrin, B.., Tolstikhin, I.N., 1984. Collection and Preparation of Natural Helium Samples for Mass-Spectrometric Analysis. pp. 1–19. https://doi.org/10.1016/B978-0-444-42180-7.50005-3

Marty, B., Dauphas, N., 2003. The nitrogen record of crust–mantle interaction and mantle convection from Archean to Present. Earth Planet. Sci. Lett. 206, 397–410. https://doi.org/10.1016/S0012-821X(02)01108-1

Marty, B., Zimmermann, L. and Humbert, F., 1996, March. Nitrogen isotopic composition of the silicate Earth and its bearing on Earth-atmosphere evolution. In Lunar and Planetary Science Conference (Vol. 27).

Matsuda, J., Marty, B., 1995. The $^{40}Ar/^{36}Ar$ ratio of the undepleted mantle; A reevaluation. Geophys. Res. Lett. 22, 1937–1940. https://doi.org/10.1029/95GL01893

Mazor, E., 1972. Paleotemperatures and other hydrological parameters deduced from noble gases dissolved in groundwaters; Jordan Rift Valley, Israel. Geochimica et Cosmochimica Acta 36, 1321–1336. https://doi.org/10.1016/0016-7037(72)90065-8

Merrill, M.D., Hunt, A.G., Lohr, C.D., 2014. Noble gas geochemistry investigation of high CO2 natural gas at the LaBarge Platform, Wyoming, USA. Energy Procedia 63, 4186–4190.

https://doi.org/10.1016/j.egypro.2014.11.451

Mitchell, E.C., Fischer, T.P., Hilton, D.R., Hauri, E.H., Shaw, A.M., de Moor, J.M., Sharp, Z.D., Kazahaya, K., 2010. Nitrogen sources and recycling at subduction zones: Insights from the Izu-Bonin-Mariana arc. Geochemistry, Geophys. Geosystems 11, n/a-n/a. https://doi.org/10.1029/2009GC002783

Moor, J.M. De, Fischer, T.P., Sharp, Z.D., Hilton, D.R., Barry, P.H., Mangasini, F., Ramirez, C., 2013. Gas chemistry and nitrogen isotope compositions of cold mantle gases from Rungwe Volcanic Province , southern Tanzania 339, 30–42.

Morley, C.K., Vanhauwaert, P., De Batist, M., 2000. Evidence for high-frequency cyclic fault activity from high-resolution seismic reflection survey, Rukwa Rift, Tanzania. J. Geol. Soc. London. 157, 983–994. https://doi.org/10.1144/jgs.157.5.983

Mtelela, C., 2016. Sedimentology and stratigraphy of the late Cenozoic lake beds succession, Rukwa Rift Basin, Tanzania: implications for hydrocarbon prospectivity. PhD thesis, James Cook University.

Muirhead, J.D., Fischer, T.P., Oliva, S.J., Laizer, A., van Wijk, J., Currie, C.A., Lee, H., Judd, E.J., Kazimoto, E., Sano, Y., Takahata, N., Tiberi, C., Foley, S.F., Dufek, J., Reiss, M.C., Ebinger, C.J., 2020. Displaced cratonic mantle concentrates deep carbon during continental rifting. Nature 582, 67–72. https://doi.org/10.1038/s41586-020-2328-3

Nagao, K., Takaoka, N., Matsubayashi, O., 1981. Rare gas isotopic compositions in natural gases of Japan. Earth Planet. Sci. Lett. 53, 175–188. https://doi.org/10.1016/0012-821X(81)90152-7

Niedermann, S., Graf, T., Marti, K., 1993. Mass spectrometric identification of cosmic-ray-produced neon in terrestrial rocks with multiple neon components. Earth Planet. Sci. Lett. 118, 65–73. https://doi.org/10.1016/0012-821X(93)90159-7

Ozima, M., Podosek, F.A., 1983. Noble Gas Geochemistry Noble. Press Syndicate of the University of Cambridge.

Pik, R., Marty, B., Hilton, D.R., 2006. How many mantle plumes in Africa? The geochemical point of view. Chem. Geol. 226, 100–114. https://doi.org/10.1016/j.chemgeo.2005.09.016

Pinti, D.L., Marty, B., 1995. Noble gases in crude oils from the Paris Basin, France: Implications for the origin of fluids and constraints on oil-water-gas interactions. Geochim. Cosmochim. Acta 59, 3389–3404. https://doi.org/10.1016/0016-7037(95)00213-J

Podosek, F.A., Bernatowicz, T.J., Kramer, F.E., 1981. Adsorption of xenon and krypton on shales. Geochimica et Cosmochimica Acta 45, 2401–2415. https://doi.org/10.1016/0016-7037(81)90094-6

Reiners, P.W., 2005. Zircon (U-Th)/He Thermochronometry. Rev. Mineral. Geochemistry 58, 151–179. https://doi.org/10.2138/rmg.2005.58.6

Roberts, E.M., O'Connor, P.M., Stevens, N.J., Gottfried, M.D., Jinnah, Z.A., Ngasala, S., Choh, A.M., Armstrong, R.A., 2010. Sedimentology and depositional environments of the Red Sandstone Group, Rukwa Rift Basin, southwestern Tanzania: New insight into Cretaceous and Paleogene terrestrial ecosystems and tectonics in sub-equatorial Africa. J. African Earth Sci. 57, 179–212. https://doi.org/10.1016/j.jafrearsci.2009.09.002

Rudnick, R.L., Fountain, D.M., 1995. Nature and composition of the continental crust: A lower crustal perspective. Rev. Geophys. 33, 267. https://doi.org/10.1029/95RG01302

Sano, Y., Wakita, H., Sheng, X., 1988. Atmospheric helium isotope ratio. Geochem. J. 22, 177–181. https://doi.org/10.2343/geochemj.22.177

Sarda, P., Staudacher, T., Allègre, C.J., 1988. Neon isotopes in submarine basalts. Earth Planet. Sci. Lett. 91, 73–88. https://doi.org/10.1016/0012-821X(88)90152-5

Stuart, F. M., Lass-Evans, S., Fitton, J. G., & Ellam, R. M. 2003. High 3 He/4 He ratios in picritic basalts from Baffin Island and the role of a mixed reservoir in mantle plumes. *Nature*, *424*(6944), 57-59.

Silver, B.J., Raymond, R., Sigman, D.M., Prokopeko, M., Sherwood Lollar, B., Lacrampe-

Couloume, G., Fogel, M.L., Pratt, L.M., Lefticariu, L., Onstott, T.C., 2012. The origin of $NO_3^-$ and $N_2$ in deep subsurface fracture water of South Africa. Chem. Geol. 294–295, 51–62. https://doi.org/10.1016/j.chemgeo.2011.11.017

Sleep, N.H., Zoback, M.D., 2007. Did Earthquakes Keep the Early Crust Habitable? Astrobiology 7, 1023–1032. https://doi.org/10.1089/ast.2006.0091

Sklyarov, E.V., Theunissen, K., Melnikov, A.I., Klerkx, J., Gladkochub, D.P., Mruma, A., 1998. Paleoproterozoic eclogites and garnet pyroxenites of the Ubende Belt (Tanzania). Schweizerische Mineralogische Petrographische Mitteilungen 78,257–271.

Smith, D.M., Goodwin, T.W., Schillinger, J.A., 2004. Challenges to the Worldwide Supply of Helium in the Next Decade, in: AIP Conference Proceedings. AIP, pp. 119–138. https://doi.org/10.1063/1.1774674

Smirnov, V., Pentelkov, V., Tolochko, V., Trifan, M., Zhukov, S., 1973. Geology and minerals of the central part of the western rift. Tech. rep., Mineral and Resource Division, Dodoma, Tanzania. Unpublished report of the geological mapping.

Sundal, A., Weber, U., Brennwald, M., Ringrose, P., Flø, N., Johnsen, K., Faramarzi, L., Aagaard, P., Kipfer, R., 2020. Monitoring Real Time, In-Line Variations of Noble Gas Concentrations During CO2 Capture Operations by Means of a Portable Mass Spectrometer. SSRN Electron. J. https://doi.org/10.2139/ssrn.3366166

Taylor, S.R. and McLennan, S.M., 1985. The continental crust: its composition and evolution.

Tedesco, D., Nagao, K., 1996. Radiogenic 4He, 21Ne and 40Ar in fumarolic gases on Vulcano: implication for the presence of continental crust beneath the island. Earth Planet. Sci. Lett. 144, 517–528. https://doi.org/10.1016/S0012-821X(96)00196-3

Tedesco, D., Nagao, K., Scarsi, P., 1998. Noble gas isotopic ratios from historical lavas and fumaroles at Mount Vesuvius (southern Italy): Constraints for current and future volcanic activity. Earth Planet. Sci. Lett. 164, 61–78. https://doi.org/10.1016/S0012-821X(98)00167-8

Tolstikhin, I.N., 1975. Helium isotopes in the earth's interior and in the atmosphere: A degassing model of the earth. Earth Planet. Sci. Lett. 26, 88–96. https://doi.org/10.1016/0012-821X(75)90180-6

Torgersen, T., 1989. Terrestrial helium degassing fluxes and the atmospheric helium budget: Implications with respect to the degassing processes of continental crust. Chem. Geol. Isot. Geosci. Sect. 79, 1–14. https://doi.org/10.1016/0168-9622(89)90002-X

Torgersen, T., 2010. Continental degassing flux of $^{4}$He and its variability. Geochemistry, Geophys. Geosystems 11, n/a-n/a. https://doi.org/10.1029/2009GC002930

Torgersen, T., Clarke, W.B., 1985. Helium accumulation in groundwater, I: An evaluation of sources and the continental flux of crustal 4He in the Great Artesian Basin, Australia. Geochim. Cosmochim. Acta 49, 1211–1218. https://doi.org/10.1016/0016-7037(85)90011-0

Torgersen, T., Ivey, G.., 1985. Helium accumulation in groundwater. II: A model for the accumulation of the crustal 4He degassing flux. Geochim. Cosmochim. Acta 49, 2445–2452. https://doi.org/10.1016/0016-7037(85)90244-3

Torgersen, T., Kennedy, B.M., 1999. Air-Xe enrichments in Elk Hills oil field gases: role of water in migration and storage. Earth Planet. Sci. Lett. 167, 239–253. https://doi.org/10.1016/S0012-821X(99)00021-7

Tyne, R.L., Barry, P.H., Karolytė, R., Byrne, D.J., Kulongoski, J.T., Hillegonds, D.J., Ballentine, C.J., *in review this issue*. Investigating the effect of enhanced oil recovery on the noble gas signature of casing gases and produced waters from selected California oil fields. Chemical Geology.

Warr, O., Giunta, T., Ballentine, C.J., Sherwood Lollar, B., 2019. Mechanisms and rates of $^{4}$He, $^{40}$Ar, and $H_2$ production and accumulation in fracture fluids in Precambrian Shield environments. Chem. Geol. 530, 119322. https://doi.org/10.1016/j.chemgeo.2019.119322

Warr, O., Sherwood, B., Fellowes, J., Sutcliffe, C.N., Mcdermott, J.M., Holland, G., Mabry,

J.C., Ballentine, C.J., 2018a. ScienceDirect Tracing ancient hydrogeological fracture network age and compartmentalisation using noble gases. Geochim. Cosmochim. Acta 222, 340–362. https://doi.org/10.1016/j.gca.2017.10.022

Weinlich, F.H., Bräuer, K., Kämpf, H., Strauch, G., Tesař, J., Weise, S.M., 1999. An active subcontinental mantle volatile system in the western Eger rift, Central Europe: gas flux, isotopic (He, C, and N) and compositional fingerprints. Geochim. Cosmochim. Acta 63, 3653–3671. https://doi.org/10.1016/S0016-7037(99)00187-8

Wescott, W.A., Krebs, W.N., Engelhardt, D.W., Cunningham, S.M., 1991. New Biostratigraphic Age Dates from the Lake Rukwa Rift Basin in Western Tanzania: Geologic Note (1). Am. Assoc. Pet. Geol. Bull. 75. https://doi.org/10.1306/0C9B2925-1710-11D7-8645000102C1865D

Williams, C.D., Mukhopadhyay, S., 2019. Capture of nebular gases during Earth's accretion is preserved in deep-mantle neon. Nature 565, 78–81. https://doi.org/10.1038/s41586-018-0771-1

Yatsevich, I., Honda, M., 1997. Production of nucleogenic neon in the Earth from natural radioactive decay. J. Geophys. Res. Solid Earth 102, 10291–10298. https://doi.org/10.1029/97JB00395

Zaikowski, A., Spangler, R.R., 1990. Noble gas and methane partitioning from groundwater: An aid to natural gas exploration and reservoir evaluation. Geology 18, 72. https://doi.org/10.1130/0091-7613(1990)018

Zartman, R.E., Wasserburg, G.J., Reynolds, J.H., 1961. Helium, argon, and carbon in some natural gases. J. Geophys. Res. 66, 277–306. https://doi.org/10.1029/JZ066i001p00277

Zimmer, M.M., Fischer, T.P., Hilton, D.R., Alvarado, G.E., Sharp, Z.D., Walker, J.A., 2004. Nitrogen systematics and gas fluxes of subduction zones: Insights from Costa Rica arc volatiles. Geochemistry, Geophys. Geosystems 5. https://doi.org/10.1029/2003GC000651

Zhou, Z., Ballentine, C.J., Kipfer, R., Schoell, M., Thibodeaux, S., 2005. Noble gas tracing of groundwater/coalbed methane interaction in the San Juan Basin, USA. Geochim. Cosmochim.

Acta 69, 5413–5428. https://doi.org/10.1016/j.gca.2005.06.027

Zhou, Z., Ballentine, C.J., Schoell, M., Stevens, S.H., 2012. Identifying and quantifying natural CO2 sequestration processes over geological timescales: The Jackson Dome CO2 Deposit, USA. Geochim. Cosmochim. Acta 86, 257–275. https://doi.org/10.1016/j.gca.2012.02.028

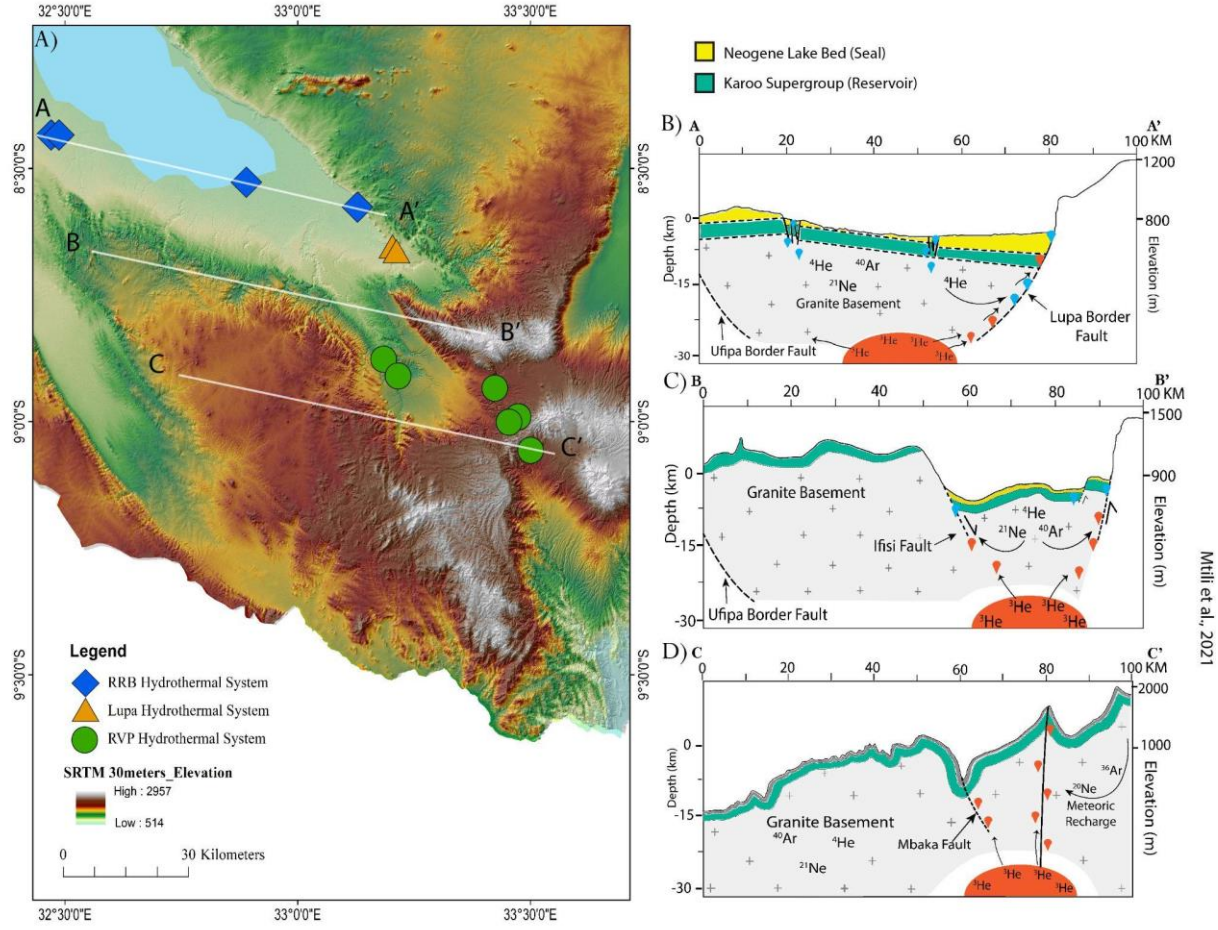


**Supplementary Figure 1. A.** Digital Elevation Model (DEM) for the area covering study area from Rukwa Rift Basin to the Rungwe Volcanic Province. **B, C, D**. Conceptual Model for the origin of helium gas across Rukwa Rift Basin, Lupa Hydrothermal System and Rungwe Volcanic Province. Thickness of the rock layers has been exaggerated to aid visibility. Structural interpretation adapted from (Heilman et al.,2018).

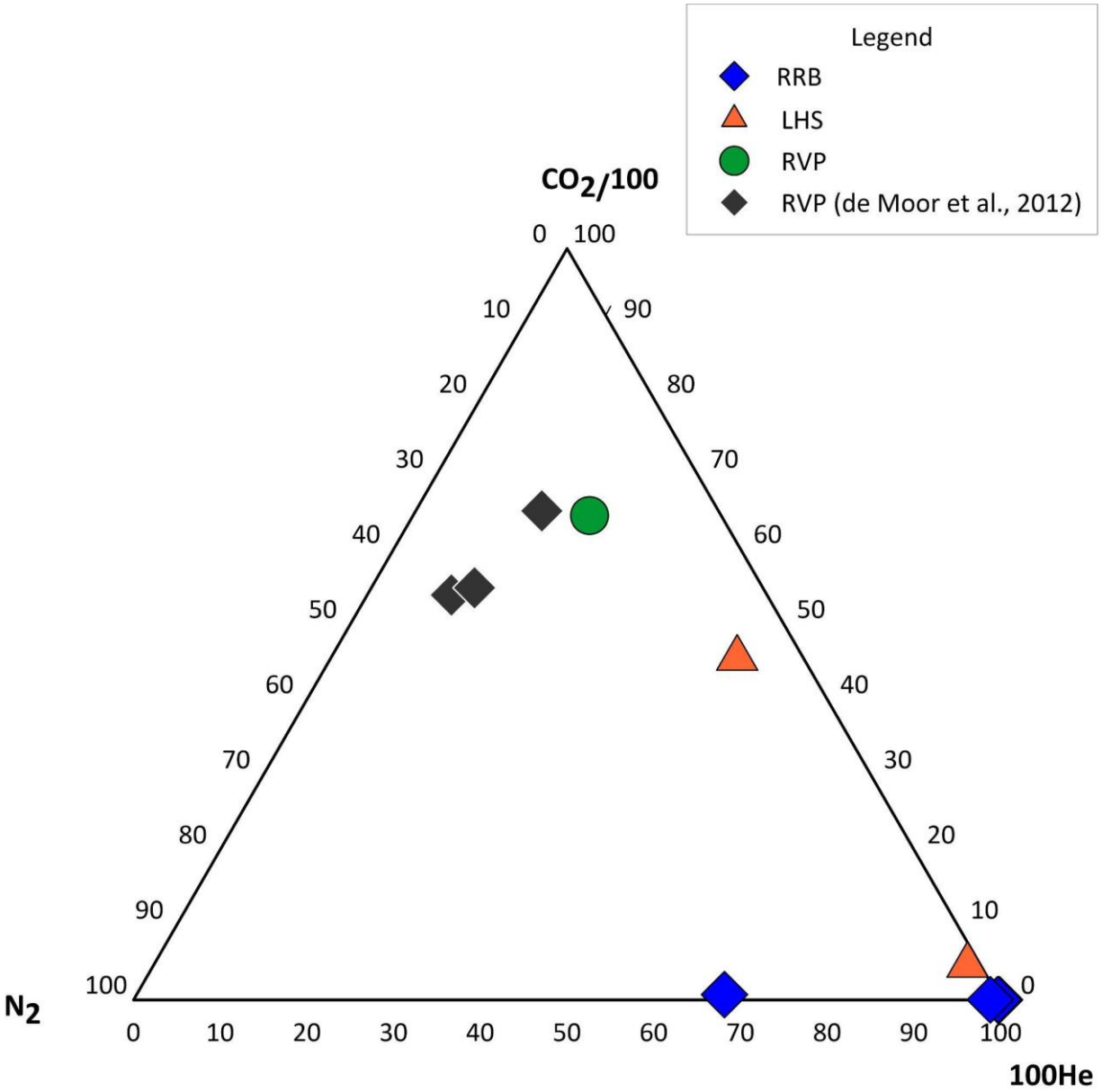


**Supplementary Figure 2.** Ternary plot of $CO_2$-$^4He$-$N_2$ showing the relative abundances of southwestern Tanzania gas seeps. Samples from RVP (de Moor et al., 2012) have been added as a reference.

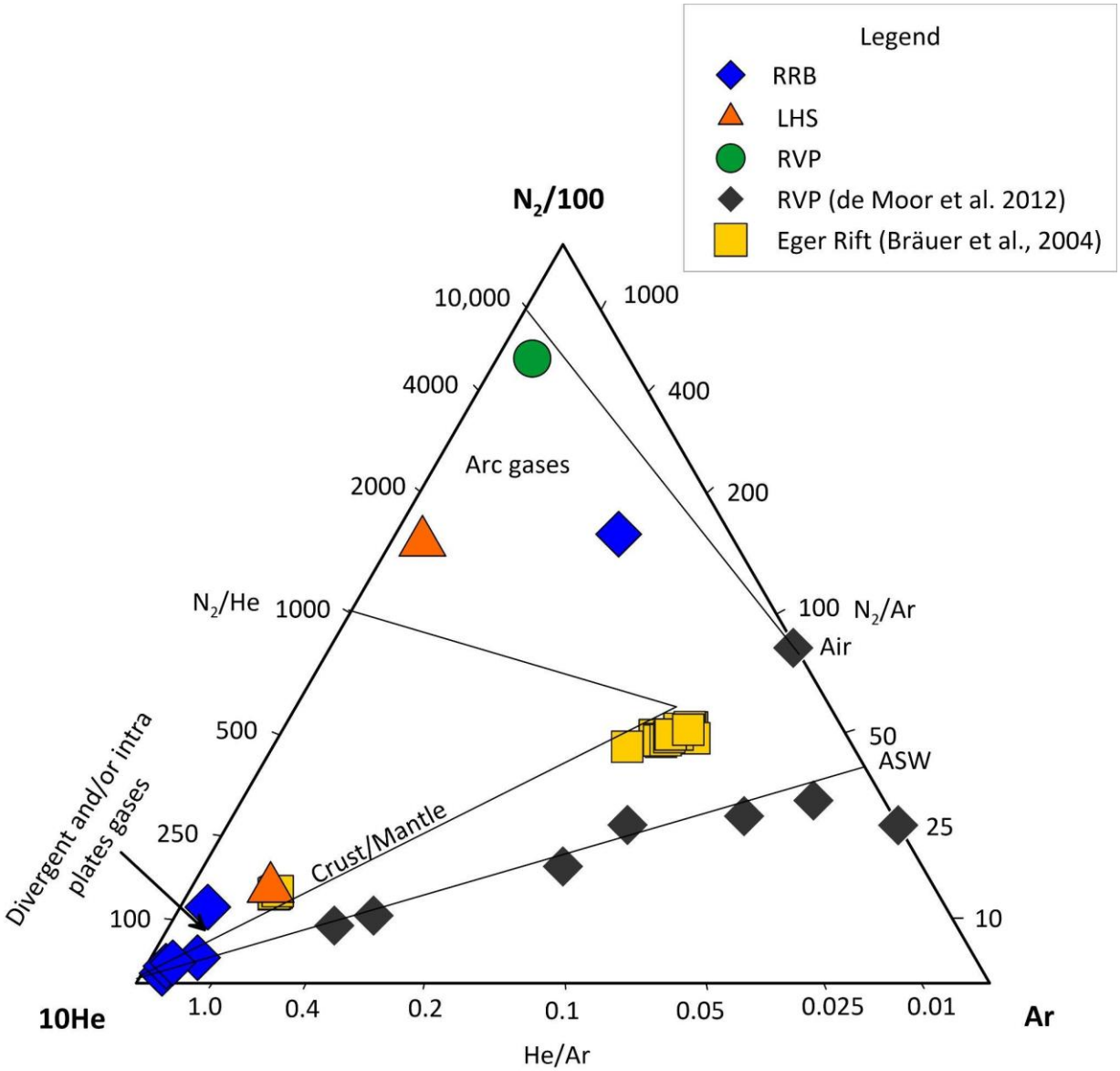


**Supplementary Figure 3.** $N_2$-He-Ar Ternary plot with endmember fields for crust/mantle, together with Air and Air Saturated Water (ASW) values. Samples from Rukwa Rift Basin (RRB) Hydrothermal System plot on a well-defined mixing line between divergent and/or intra plate gases He apex and ASW. Compositional data from Rungwe Volcanic Province (RVP; de Moor et al,. 2013) and Eger Rift (Bräuer et al., 2004) are plotted for reference. Nitrogen concentrations were measured on the portable mass spectrometer (miniRuedi)

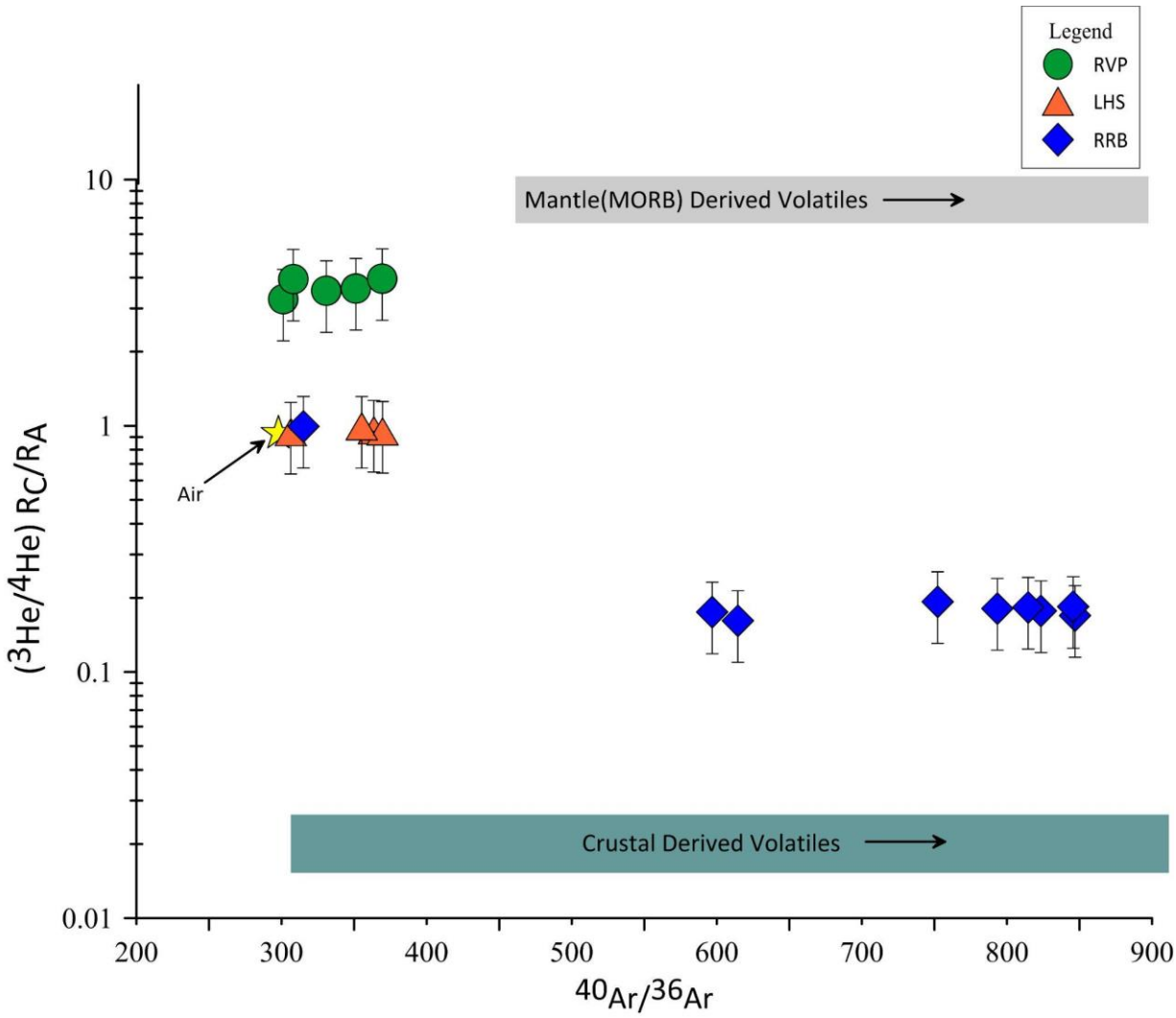


**Supplementary Figure 4:** Air corrected $^{3}He/^{4}He$ ratio vs $^{40}Ar/^{36}Ar$. 1 sigma errors are shown. Atmospheric, crustal and mantle endmembers have been added for reference. A significant difference is observed in the different regions.

Table 1a. Noble gas isotope data for RRB, LHS and RVP (from Static Mass Spectrometer).

| Sample Id | Spring Name | Latitude (˚S) | Longitude (˚E) | [$^{4}$He] $\times10^{-6}$ | | $^{4}$He% | [$^{20}$Ne] $\times10^{-9}$ | | [$^{40}$Ar] $\times10^{-6}$ | | $^{40}$Ar/$^{36}$Ar | | X-value[a] | | $R_C/R_A$[b] | |
|---|---|---|---|---|---|---|---|---|---|---|---|---|---|---|---|---|
| ***Rukwa Rift Basin (RRB)*** | | | | | | | | | | | | | | | | |
| TZ181309S5 (801) | Ivuna mudpots-1 | 08°25.538' | 32°28.460' | 25200 | (200) | 2.5 | 12100 | (200) | 15400 | (1000) | 614.5 | (5.9) | 6520 | (30) | 0.16 | (0.05) |
| TZ181309S5 (849) | Ivuna mudpots-1 Du | 08°25.538' | 32°28.460' | 24400 | (200) | 2.4 | 11400 | (200) | 15500 | (1000) | 596.9 | (5.8) | 6680 | (30) | 0.18 | (0.06) |
| TZ181309S6 (802) | Ivuna mudpots-2 | 08°25.538' | 32°28.460' | 67900 | (600) | 6.8 | 7250 | (100) | 17200 | (1100) | 846.9 | (8.2) | 29400 | (100) | 0.17 | (0.05) |
| TZ181309S6 (854) | Ivuna mudpots-2 Du | 08°25.538' | 32°28.460' | 69300 | (300) | 6.9 | 7060 | (90) | 16600 | (1000) | 845.7 | (8.2) | 30800 | (100) | 0.18 | (0.06) |
| TZ181409S7 (851) | Itumbula salt pond-1 | 08°25.850' | 32°28.858' | 36000 | (400) | 3.6 | 3090 | (40) | 9450 | (590) | 752.2 | (7.3) | 36500 | (100) | 0.19 | (0.06) |
| TZ181409S7 (852) | Itumbula salt pond-1 Dup | 08°25.850' | 32°28.858' | 39400 | (300) | 3.9 | 4330 | (60) | 10500 | (700) | 823.4 | (7.9) | 28600 | (100) | 0.18 | (0.06) |
| TZ181409S8 (805) | Itumbula salt pond-2 | 08°25.850' | 32°28.858' | 31900 | (300) | 3.2 | 3630 | (50) | 9910 | (620) | 793.4 | (7.7) | 27600 | (100) | 0.18 | (0.06) |
| TZ18140958 (853) | Itumbula salt pond-2 Dup | 08°25.850' | 32°28.858' | 28800 | (300) | 2.9 | 3180 | (40) | 8480 | (530) | 814.6 | (7.9) | 28400 | (100) | 0.18 | (0.06) |
| TZ180511S31 (831) | Kajundu Spring | 08°31.027' | 32°53.361' | 218 | (2) | 0.02 | 5810 | (80) | 3990 | (250) | 315 | (3) | 1180 | (10) | 0.99 | (0.32) |
| TZ180610S23 (823) | Tete Spring | 08°34.003' | 33°07.732' | 7650 | (70) | 0.8 | 4290 | (60) | 3100 | (190) | 298.1 | (2.9) | 5590 | (20) | 0.26 | (0.08) |
| ***Lupa Hydrothermal System (LHS)*** | | | | | | | | | | | | | | | | |

| | | | | | | | | | | | | | | | | |
|---|---|---|---|---|---|---|---|---|---|---|---|---|---|---|---|---|
| TZ181910S26 (826) | Ibaya Spring-1 | 08°39.414' | 33°12.189' | 86.3 | (0.8) | 0.01 | 55.2 | (0.7) | 87.6 | (5.5) | 306.4 | (2.9) | 4900 | (20) | 0.94 | (0.304) |
| TZ181910S27 (827) | Ibaya Spring-2 | 08°39.418' | 33°12.191' | 86.0 | (0.8) | 0.01 | 41.8 | (0.6) | 74.9 | (4.7) | 363.6 | (3.5) | 6450 | (30) | 0.96 | (0.31) |
| TZ180411S29 (829) | Ngwilo Spring-1 | 08°39.833' | 33°12.649' | 1480 | (10) | 0.15 | 1090 | (10) | 1770 | (110) | 369.6 | (3.6) | 4250 | (20) | 0.95 | (0.31) |
| TZ180411S30 (835) | Ngwilo Spring-2 | 08°39.873' | 33°12.690' | 649 | (6) | 0.06 | 487 | (7) | 973 | (61) | 355.3 | (3.4) | 4190 | (20) | 0.99 | (0.32) |
| ***Rungwe Volcanic Province (RVP)*** | | | | | | | | | | | | | | | | |
| **Ngozi-Songwe Hydrothermal system** | | | | | | | | | | | | | | | | |
| TZ180410S21 (820) | Nanyara Spring-1 | 08°52.279' | 33°11.090' | 14.9 | (0.1) | 0.00149 | 33.4 | (0.5) | 46.9 | (2.9) | 351.3 | (3.4) | 1400 | (10) | 3.62 | (1.17) |
| TZ180410S21 (836) | Nanyara Spring-1 Dup | 08°52.279' | 33°11.090' | 24.6 | (0.2) | 0.00246 | 59.7 | (0.8) | 89.4 | (5.6) | 369.4 | (3.6) | 1290 | (10) | 3.95 | (1.28) |
| TZ180410S22 (822) | Nanyara Spring-2 | 08°52.240' | 33°11.103' | 0.115 | (0.001) | 0.00001 | 82.3 | (1.1) | 84.2 | (5.3) | n.d | | 4.39 | (0.02) | 3.53 | (1.14) |
| TZ181109S3 (799) | Songwe river-1 | 08°54.212' | 33°12.971' | 1.07 | (0.01) | 0.00011 | 30.4 | (0.4) | 59.3 | (3.7) | 330.9 | (3.2) | 111 | (1) | 3.54 | (1.14) |
| TZ181109S3 (843) | Songwe river-1 Dup | 08°54.212' | 33°12.971' | 0.449 | (0.004) | 0.00004 | 8.9 | (0.1) | 11.7 | (0.7) | n.d | | 157 | (1) | 4.00 | (1.29) |
| TZ181109S4 (800) | Songwe river-2 | 08°54.258' | 33°12.936' | 0.799 | (0.008) | 0.00008 | 8.6 | (0.1) | 20.8 | (1.3) | 301.2 | (2.9) | 291 | (1) | 3.27 | (1.05) |
| TZ181109S4 (842) | Songwe river-2 Dup | 08°54.258' | 33°12.936' | 0.813 | (0.008) | 0.00008 | 8.5 | (0.1) | 18.1 | (1.1) | 308.1 | (2.9) | 299 | (1) | 3.93 | (1.27) |

[a] X-value = ($^{4}He/^{20}Ne$)measured/($^{4}He/^{20}Ne$)air.

[b] $R_C/R_A$ is the air corrected He isotope ratio=$[(R/R_A \times X) - 1]/ (X - 1)$.

Table 1b. Noble gas isotope ratios data for RRB, LHS and RVP.

| Sample Id | Spring Name | Temp. ($^0$C) | Specific Cond. ($\mu S^{-1}$) | pH | $^{20}Ne/^{21}Ne$ | | $^{21}Ne/^{22}Ne$ | | $^4He/^{40}Ar^*$ | | $CO_2/^3He$ |
|---|---|---|---|---|---|---|---|---|---|---|---|
| ***Rukwa Rift Basin (RRB)*** | | | | | | | | | | | |
| TZ181309S5 (801) | Ivuna mudpots-1 | 31.7 | 6247 | 6.86 | 9.72 | (0.08) | 0.0302 | (0.0012) | 3.2 | (0.4) | 2.39E+06 |
| TZ181309S5 (849) | Ivuna mudpots-1 Dup | | | | 9.77 | (0.08) | 0.0307 | (0.0012) | 3.1 | (0.4) | - |
| TZ181309S6 (802) | Ivuna mudpots-2 | 31.7 | 6247 | 6.86 | 9.64 | (0.08) | 0.0322 | (0.0013) | 6.1 | (0.7) | 8.75E+05 |
| TZ181309S6 (854) | Ivuna mudpots-2 Dup | | | | 9.67 | (0.08) | 0.0323 | (0.0013) | 6.4 | (0.7) | - |
| TZ181409S7 (851) | Itumbula salt pond-1 | 50.1 | 4759.9 | 9.2 | 9.36 | (0.08) | 0.0333 | (0.0013) | 6.3 | (0.7) | 1.14E+06 |
| TZ181409S7 (852) | Itumbula salt pond-1 Du | | | | 9.70 | (0.08) | 0.0322 | (0.0013) | 5.9 | (0.7) | - |
| TZ181409S8 (805) | Itumbula salt pond-2 | 50.1 | 4759.9 | 9.2 | 9.75 | (0.08) | 0.0321 | (0.0013) | 5.2 | (0.6) | 1.62E+06 |
| TZ181409S8 (853) | Itumbula salt pond-2 Du | | | | 9.76 | (0.08) | 0.0322 | (0.0013) | 5.4 | (0.6) | - |
| TZ180511S31 (831) | Kajundu Spring | 29.5 | 2697 | 8.63 | 9.66 | (0.08) | 0.0289 | (0.0012) | 1.04 | (0.12) | 9.40E+07 |
| TZ180610S23 (823) | Tete Spring | 42 | 1477 | 8.37 | 9.73 | (0.08) | 0.0292 | (0.0012) | - | | 8.79E+06 |
| ***Lupa Hydrothermal System (LHS)*** | | | | | | | | | | | |
| TZ181910S26 (826) | Ibaya Spring-1 | 81.7 | 3138 | 7.14 | 10.01 | (0.08) | 0.0296 | (0.0012) | 38.5 | (4.3) | 1.02E+10 |
| TZ181910S27 (827) | Ibaya Spring-2 | | | | 9.91 | (0.08) | 0.0276 | (0.0012) | 6.4 | (0.7) | - |
| TZ180411S29 (829) | Ngwilo Spring-1 | 54.6 | 3146 | 6.99 | 9.70 | (0.08) | 0.0295 | (0.0012) | 4.3 | (0.5) | 5.11E+08 |

| | | | | | | | | | | | |
|---|---|---|---|---|---|---|---|---|---|---|---|
| TZ180411S30 (835) | Ngwilo Spring-2 | 78.6 | 3204 | 7.46 | 9.78 | (0.08) | 0.0294 | (0.0012) | 4.2 | (0.5) | - |
| ***Rungwe Volcanic Province (RVP)*** | | | | | | | | | | | |
| **Ngozi-Songwe Hydrothermal system** | | | | | | | | | | | |
| TZ180410S21 (820) | Nanyara Spring-1 | 38.6 | 3805 | 6.8 | 9.99 | (0.08) | 0.0293 | (0.0012) | 2.1 | (0.1) | - |
| TZ180410S21 (836) | Nanyara Spring-1 Dup | 38.6 | 3805 | 6.8 | 9.97 | (0.08) | 0.0294 | (0.0012) | 1.4 | (0.2) | - |
| TZ180410S22 (822) | Nanyara Spring-2 | - | - | | 9.83 | (0.08) | 0.02904 | (0.00116) | - | | - |
| TZ181109S3 (799) | Songwe river-1 | 45.6 | 4045 | 6.47 | 9.86 | (0.08) | 0.02835 | (0.00113) | 0.18 | (0.01) | |
| TZ181109S3 (843) | Songwe river-1 Dup | 45.6 | 4045 | 6.47 | 9.91 | (0.08) | 0.0287 | (0.0012) | - | | 6.42E+10 |
| TZ181109S4 (800) | Songwe river-2 | 56 | 4018 | 6.56 | 9.93 | (0.08) | 0.0288 | (0.0012) | 4.3 | (0.3) | - |
| TZ181109S4 (842) | Songwe river-2 Dup | 56 | 4018 | 6.56 | 9.87 | (0.08) | 0.0291 | (0.0012) | 1.5 | (0.2) | - |

Table 2. Bulk composition data for the RRB, LHS and RVP (from the mini ruedi)

| Sample Id | Spring Name | $N_2$% | | $^4$He% | | $^{40}$Ar% | | $CO_2$% | | $O_2$% | | $N_2/^4He^a$ | $N_2/^{40}Ar^a$ | $^4He^a/^{40}Ar^a$ |
|---|---|---|---|---|---|---|---|---|---|---|---|---|---|---|
| ***Rukwa Rift Basin (RRB)*** | | | | | | | | | | | | | | |
| TZ181309S5 (801) | Ivuna mudpots-1 | 94.1 | (0.5) | 2.663 | (0.02) | 1.60 | (0.01) | 0.986 | (0.091) | 3.07 | (0.01) | 37.6 | 62.7 | 1.64 |
| TZ181309S6 (802) | Ivuna mudpots-2 | 94.0 | (0.4) | 2.25 | (0.03) | 1.95 | (0.01) | 1.29 | (0.10) | 3.09 | (0.01) | 13.6 | 55.3 | 3.94 |
| TZ181409S7 (852) | Itumbula salt pond-1 | 94.4 | (0.4) | 4.24 | (0.04) | 1.58 | (0.01) | 0.801 | (0.077) | 2.76 | (0.01) | 24.2 | 99.4 | 3.76 |
| TZ181409S8 (805) | Itumbula salt pond-2 | 93.0 | (0.4) | 4.06 | (0.06) | 1.87 | (0.01) | 0.947 | (0.094) | 4.10 | (0.02) | 29.1 | 93.9 | 3.22 |

| | | | | | | | | | | | | | | |
|---|---|---|---|---|---|---|---|---|---|---|---|---|---|---|
| TZ180511S31 (831) | Kajundu Spring | 93.0 | (0.4) | 0.056 | (0.001) | 1.02 | (0.01) | 2.07 | (0.22) | 3.47 | (0.02) | 4650 | 233 | 0.05 |
| TZ180610S23 (823) | Tete Spring | 95.1 | (0.4) | 2.61 | (0.05) | 1.79 | (0.01) | 1.77 | (0.19) | 1.65 | (0.01) | 119 | 317 | 2.47 |
| ***Lupa Hydrothermal System (LHS)*** | | | | | | | | | | | | | | |
| TZ181910S26 (826) | Ibaya Spring-1 | 14.1 | (0.1) | 0.061 | (0.001) | 0.367 | (0.002) | 83.7 | (9.0) | 1.98 | (0.01) | 1630 | 1600 | 0.99 |
| TZ180411S29 (829) | Ngwilo Spring-1 | 24.3 | (0.1) | 0.26 | (0.01) | 0.605 | (0.003) | 72.4 | (8.0) | 2.80 | (0.01) | 164 | 137 | 0.83 |
| ***Rungwe Volcanic Province (RVP)*** | | | | | | | | | | | | | | |
| TZ181109S3 (843) | Nanyara Spring-1 | 18.3 | (0.2) | 0.00028 | (1.00E-05) | 0.141 | (0.001) | 77.9 | (0.6) | 3.66 | (0.04) | 7460 | 2050 | 0.04 |

[a] Noble gas concentrations were taken from the measurements in the Noble Laboratory, Oxford (Table 1a)

Table 3. Calculated Vg/Vw values for samples using both $^{36}Ar$ and $^{20}Ne$.

| Sample Id | | Vg/Vw($^{36}Ar$) | Vg/Vw ($^{20}Ne$) |
|---|---|---|---|
| ***(RRB)*** | | | |
| TZ181309S5 | Ivuna mudpots-1 | 0.003 | 0.003 |
| TZ181309S5 | Ivuna mudpots-1 dup | 0.001 | 0.004 |
| TZ181309S6 | Ivuna mudpots-2 | 0.012 | 0.012 |
| TZ181309S6 | Ivuna mudpots-2 dup | 0.014 | 0.013 |
| TZ181409S7 | Itumbula salt pond-1 | 0.044 | 0.044 |
| TZ181409S7 | Itumbula salt pond-1 dup | 0.043 | 0.028 |
| TZ181409S8 | Itumbula salt pond-2 | 0.045 | 0.036 |
| TZ181409S8 | Itumbula salt pond-2 dup | 0.061 | 0.043 |
| TZ180511S31 | Kajundu Spring | 0.044 | 0.018 |
| TZ180610S23 | Tete Spring | 0.062 | 0.029 |
| ***(LHS)*** | | | |
| TZ181910S26 | Ibaya Spring-1 | 3.612 | 3.106 |
| TZ181910S27 | Ibaya Spring-2 | 5.028 | 4.101 |

| | | | |
|---|---|---|---|
| TZ180411S29 | Ngwilo Spring-1 | 0.179 | 0.146 |
| TZ180411S30 | Ngwilo Spring-2 | 0.342 | 0.342 |
| ***(RVP)*** | | | |
| TZ180410S21 | Nanyara Spring-1 | 4.272 | 2.867 |
| TZ180410S22 | Nanyara Spring-2 | 3.493 | 2.079 |
| TZ181109S3 | Songwe river-1 | 23.214 | 19.177 |
| TZ181109S4 | Songwe river-2 | 17.773 | 20.160 |

Table 4. $CO_2$, He and crustal $^4He$ flux in southwestern Tanzania

| | Hydrothermal System | $Q_{CO2}$ (t $d^{-1}$)[a] | $Q_{He}$ (mol $yr^{-1}$)[b] | $R/Ra$[c] | $q^{C}_{He}$ (1) (mol $yr^{-1}$)[d] | $q^{C}_{He}$ (2) (mol $yr^{-1}$)[e] | WC (1)[f] | WC (2)[g] |
|---|---|---|---|---|---|---|---|---|
| Based on Lee et al., 2016 $CO_2$ flux estimates | RRB | 1.63E+04 | 2.85E+10 | 0.19 | 2.82E+10 | 2.79E+10 | 620000 | 616000 |
| | LHS | 4.30E+03 | 4.96E+06 | 0.96 | 4.64E+06 | 4.37E+06 | 102 | 96.4 |
| | RVP | 5.19E+03 | 1.30E+05 | 3.60 | 9.89E+04 | 7.16E+04 | 2.2 | 1.6 |
| Based on Barry et al., 2013 $CO_2$ flux estimates | RRB | 1.45E+01 | 2.54E+7 | 0.19 | 2.51E+7 | 2.48E+7 | 553.3 | 547.8 |
| | LHS | 3.82 | 4.40E+03 | 0.96 | 4.13E+03 | 3.88E+03 | 0.091 | 0.086 |
| | RVP | 4.61 | 1.15E+02 | 3.60 | 8.79E+01 | 6.36E+04 | 0.0019 | 0.0014 |

[a] Estimated flux of $CO_2$ in the system based on area and total $CO_2$ flux extrapolation (i.e., Barry et al., 2013; Lee et al., 2016).

[b] Calculated flux of He from $CO_2$ and measured $CO_2/^4He$.

[c] Average $^3He/^4He$ for each of the areas divided by the $^3He/^4He$ in air = $1.39 \times 10^{-6}$.

[d] Crustal $^4He$ flux assuming a mantle R/Ra value of 15 (Hilton et al., 2011).

[e] Crustal $^4$He flux assuming a mantle R/Ra value of 8 (Barry et al., 2013).

[f] Calculated crustal $^4$He flux based on $^4$He ($\boldsymbol{q^{C}_{He}}$ **(1)**) annually produced by 38-km-thick crustal area (14,000 km$^2$).

[g] Calculated crustal $^4$He flux based on $^4$He ($\boldsymbol{q^{C}_{He}}$ **(2)**) annually produced by 38-km-thick crustal area (14,000 km$^2$).